Correspondence to:
Z. Tan,
tanzh@uchicago.edu

Large-eddy simulation of subtropical cloud-topped boundary layers: 1. A forcing framework with closed surface energy balance

Zhihong Tan[1,2,3], Tapio Schneider[1,2], João Teixeira[2,4], and Kyle G. Pressel[1]

[1]Department of Earth Sciences, ETH Zürich, Zürich, Switzerland, [2]California Institute of Technology, Pasadena, California, USA, [3]Department of Geophysical Sciences, University of Chicago, Chicago, Illinois, USA, [4]Jet Propulsion Laboratory, Pasadena, California, USA

Abstract Large-eddy simulation (LES) of clouds has the potential to resolve a central question in climate dynamics, namely, how subtropical marine boundary layer (MBL) clouds respond to global warming. However, large-scale processes need to be prescribed or represented parametrically in the limited-area LES domains. It is important that the representation of large-scale processes satisfies constraints such as a closed energy balance in a manner that is realizable under climate change. For example, LES with fixed sea surface temperatures usually do not close the surface energy balance, potentially leading to spurious surface fluxes and cloud responses to climate change. Here a framework of forcing LES of subtropical MBL clouds is presented that enforces a closed surface energy balance by coupling atmospheric LES to an ocean mixed layer with a sea surface temperature (SST) that depends on radiative fluxes and sensible and latent heat fluxes at the surface. A variety of subtropical MBL cloud regimes (stratocumulus, cumulus, and stratocumulus over cumulus) are simulated successfully within this framework. However, unlike in conventional frameworks with fixed SST, feedbacks between cloud cover and SST arise, which can lead to sudden transitions between cloud regimes (e.g., stratocumulus to cumulus) as forcing parameters are varied. The simulations validate this framework for studies of MBL clouds and establish its usefulness for studies of how the clouds respond to climate change.

1. Introduction

Marine boundary layers (MBL) over subtropical oceans are often topped by low clouds, predominantly stratocumuli and cumuli [*Stevens*, 2005]. Stratocumuli (Sc) are abundant over the eastern boundaries of subtropical oceans, in the subsiding branches of the Walker and Hadley circulations and over relatively cool sea surfaces. Sc form a dense cover with high albedo exerting a strong shortwave (SW) cooling on the surface [*Wood*, 2012]. Cumuli (Cu) occur over the interiors of subtropical oceans, where subsidence is weaker and sea surfaces are warmer. Although the local albedo modification of Cu is weaker because of their lower fractional cloud cover, they occur over a much greater portion of subtropical ocean surfaces. Therefore, they are also important regulators of Earth's radiative energy budget. How these MBL clouds change as the climate warms and the large-scale conditions in which they are embedded change remains one of the central unresolved questions in climate dynamics. Uncertainties about this cloud response dominate uncertainties in climate change projections [e.g., *Cess et al.*, 1990, 1996; *Bony and Dufresne*, 2005; *Webb et al.*, 2006; *Dufresne and Bony*, 2008; *Vial et al.*, 2013; *Brient et al.*, 2015; *Brient and Schneider*, 2016].

Large-eddy simulations (LES) have the potential to reduce these uncertainties because they can explicitly simulate the dynamics of boundary layers and clouds, albeit only in a limited computational domain that typically extends at most over $O(10\,\text{km})$ in the horizontal. LES have been successful in reproducing observed boundary layers topped with Sc [*Duynkerke et al.*, 1999; *Stevens et al.*, 2005; *Caldwell and Bretherton*, 2009a] and Cu [*Siebesma et al.*, 2003; *Matheou et al.*, 2011; *vanZanten et al.*, 2011]. They have also been used to explore how Sc and Cu respond to perturbations in surface temperatures or in large-scale processes such as subsidence, which are externally prescribed in LES [e.g., *Sandu and Stevens*, 2011; *Chung et al.*, 2012; *Bellon and Stevens*, 2012; *Rieck et al.*, 2012; *Bretherton et al.*, 2013; *Bretherton*, 2015]. However, the cloud response to perturbations depends on how the large-scale processes are represented in LES, making it

difficult to compare LES results obtained under different large-scale forcing frameworks. To remedy this difficulty in comparing simulation results, the CFMIP/GASS Intercomparison of Large-Eddy and Single-Column Models (CGILS) project recently established a large-scale forcing protocol for LES at a few key locations, representing subtropical Sc, Sc-over-Cu, and Cu regimes [*Zhang et al.*, 2013]. The CGILS framework has also been used to study the cloud response to idealized climate changes, such as a 2-K warming of the surface accompanied by weakened subsidence [*Blossey et al.*, 2013; *Bretherton et al.*, 2013]. This has provided insight into the mechanisms responsible for the cloud response to climate changes [*Bretherton*, 2015].

Questions remain, however, whether the perturbations to large-scale conditions prescribed in LES represent realizable climate changes, and thus whether the cloud responses obtained in LES actually may be realized under climate change. For example, when sea surface temperatures (SST) at the lower boundary are prescribed, as is typically done in LES of subtropical MBL clouds, the surface energy balance is not closed. The ocean surface represents an infinite heat bath that can provide fluxes of latent and sensible heat irrespective of the energetic constraints that the real ocean surface would have to satisfy. Global warming is represented as a prescribed SST increase in this framework, and if the MBL relative humidity is constrained to stay constant [e.g., *Rieck et al.*, 2012], latent heat fluxes (LHF) at the surface will increase rapidly with SST, at the rate given by the Clausius-Clapeyron relation: around 6–7% per kelvin SST rise. In reality, however, LHFs at the surface are energetically constrained—radiative energy is needed to evaporate water. LHFs increase more slowly with SST than indicated by the Clausius-Clapeyron rate: at around 2–3% per kelvin SST rise [*Boer*, 1993; *Knutson and Manabe*, 1995; *Held and Soden*, 2000; *Allen and Ingram*, 2002; *Held and Soden*, 2006; *Stephens and Ellis*, 2008; *Schneider et al.*, 2010]. The excessive LHFs arising when warming is represented by an SST increase without closing the surface energy balance can severely distort the cloud response to warming, e.g., through distortions in moisture or buoyancy fluxes near the surface [e.g., *Webb and Lock*, 2013].

Here we present a framework of forcing LES that closes the surface energy balance and thus guarantees realizable changes of surface fluxes in response to climate changes. This is achieved by coupling the LES domain to a mixed-layer (slab) ocean that satisfies an energy balance equation, similar to what is commonly done in studies of large-scale dynamics with idealized general circulation models (GCMs) [e.g., *Frierson et al.*, 2006; *O'Gorman and Schneider*, 2008]. The SST is no longer prescribed but evolves in accordance with the energy balance. Thus, the SST achieved under this framework depends on energetic forcing parameters, such as the longwave opacity of the atmosphere. As a consequence, radiative transfer in the atmosphere must also be represented, as well as any large-scale energy fluxes within the atmosphere that are necessary to achieve closure of the atmospheric energy balance. In the free troposphere, we exploit the weakness of horizontal temperature gradients within the tropics [*Charney*, 1963; *Sobel et al.*, 2001] to represent the effect of large-scale energy fluxes as relaxation to a temperature profile that is representative of the convecting branch of the tropical circulation and is in radiative-convective equilibrium (RCE) with the given energetic forcing parameters (similar to *Zhang and Bretherton* [2008] and *Caldwell and Bretherton* [2009b]). This guarantees broad dynamical consistency between the warming both in the free troposphere and in the boundary layer that results, for example, when the concentration of well-mixed greenhouse gases is increased.

We test this forcing framework with the Python Cloud Large Eddy Simulation code (PyCLES) [*Pressel et al.*, 2015], coupled to the Rapid Radiative Transfer Model for GCM Applications (RRTMG) [*Iacono et al.*, 2008]. We simulate the three cases representative of subtropical Sc, Sc-over-Cu, and Cu MBL cloud regimes that were also considered under the CGILS framework. Qualitative agreement between the results under our framework and the results under CGILS verifies the capacity of the new framework to reproduce the three cloud regimes. Sensitivity tests show that the model results are relatively insensitive to the resolution and domain size, except for the Sc-over-Cu case (S11), in which transitions between Sc and Cu regimes can occur. The sensitivities of model results to perturbations in the prescribed large-scale forcings and ocean heat uptake (OHU) are also tested and discussed. Because under the new framework, SST are not fixed but adjust to rebalance the surface energy budget against imposed perturbations, feedbacks between cloud cover and SST arise and can lead to transitions between cloud regimes.

This paper is organized as follows: section 2 describes the PyCLES model and the formulation of large-scale forcings and surface boundary conditions. Section 3 describes the experimental setup of the three representative MBL cloud cases. Section 4 presents the LES results under our forcing framework and compares them with results under the original CGILS framework. Section 5 describes the MBL cloud responses to perturbed

Table 1. Comparison Between the New Forcing Framework and the CGILS Framework [*Zhang et al.*, 2013; *Blossey et al.*, 2013]

	CGILS	New Framework
Dynamical core	Differ from model to model	Anelastic, fifth-order WENO advection
Radiation	RRTMG, no diurnal cycle	Same as CGILS
Microphysics	Differ from model to model	Seifert-Beheng two-moment warm rain
Subsidence	Prescribed shape, peak at 750 hPa	Slightly different shape, peak at 667 hPa
Advection in MBL	Prescribed profiles	Same as CGILS
Advection in the free troposphere	Prescribed as residual of radiative cooling and subsidence warming	Zero
Relaxation in the free troposphere	Prescribed nudging height, $\tau = 1$ h	Relaxation height depends on boundary layer depth, $\tau = 24$ h
Moisture nudging	Up to q_{ref} below 1.3 km, $\tau = 1$ h	Up to RH=0.2 below 2.0 km, $\tau = 1$ h
Geostrophic wind	No Coriolis forcing	With Coriolis forcing, linear u_g profile
Wind nudging	Mean wind nudging, $\tau = 10$ min (all levels)	Same as scalar relaxation (only above boundary layer)
Surface fluxes	Simple bulk formula	Based on Monin-Obukhov similarity
SST	Prescribed	Interactive with prescribed OHU

large-scale forcings and OHU, highlighting the cloud cover-SST feedback arising with interactive SST. Section 6 summarizes our conclusions and their implications for studies of climate change. An appendix discusses sensitivities to the subgrid-scale (SGS) diffusion scheme. In a companion paper, we show how the new forcing framework can be used to study the response of MBL clouds to changing greenhouse gas concentrations.

2. Model and Forcing Framework

The new LES forcing framework for studying subtropical MBL clouds has some similarities with the CGILS framework [*Zhang et al.*, 2013; *Blossey et al.*, 2013], for example, in that it uses relaxation to prescribed reference profiles of temperature and specific humidity in the free troposphere, to circumvent the difficulty of achieving a closed energy balance above the MBL clouds. However, it also differs from the CGILS framework in essential respects, for example, by enforcing a closed surface energy balance with an interactive SST. Table 1 provides a side-by-side comparison between the two frameworks. Details of the LES forcing framework we use are described in what follows.

2.1. LES Code

The simulations are performed using PyCLES, which solves the moist anelastic equations of *Pauluis* [2008] with specific entropy s and total water specific humidity q_t as prognostic thermodynamic variables [*Pressel et al.*, 2015]. It uses Weighted Essentially Non-oscillatory (WENO) transport schemes [*Liu et al.*, 1994; *Jiang and Shu*, 1996; *Balsara and Shu*, 2000] for momentum and scalars on a uniform Arakawa C-grid [*Arakawa and Lamb*, 1977]. We use a fifth-order WENO scheme in this study. For time stepping, we use the strong stability preserving (SSP) second-order, two-stage Runge-Kutta (RK) method of *Shu and Osher* [1988], with adaptive time steps and with a target Courant number of 0.7.

Subgrid-scale (SGS) fluxes of momentum and scalars are computed with the Smagorinsky-Lilly closure [*Smagorinsky*, 1963; *Lilly*, 1962], with Smagorinsky coefficient $c_s = 0.23$ and a turbulent Prandtl number $Pr_t = 1/3$. Inspired by the results of K. G. Pressel et al. (Numerics and subgrid-scale modeling in large eddy simulations of stratocumulus clouds, submitted to *Journal of Advances in Modeling Earth Systems*, 2016), we have run additional simulations with zero SGS diffusivity except in the surface layer (see Appendix A for details). The momentum, entropy, and water vapor fluxes at the lower boundary are computed using standard bulk aerodynamic formulas, with near-surface fluxes determined by Monin-Obukhov similarity theory [*Byun*, 1990]. The roughness lengths of momentum and entropy (including sensible and latent heat) are $z_m = 10^{-3}$ m and 3×10^{-5} m, respectively. At the upper boundary, all fluxes (except radiative fluxes) are set to zero. A sponge layer extends over the top 500 m of the domain and linearly damps fluctuations to the domain mean (see *Pressel et al.* [2015] for details of the LES code).

2.2. Radiative Transfer

To achieve a closed energy balance at the surface, we need to model radiative transfer. To do so, we integrated RRTMG [*Iacono et al.*, 2008] into PyCLES. The LES code provides values of temperature (T), specific

humidity of water vapor (q_v), and specific humidity of cloud liquid (q_l) for the radiative transfer calculations in RRTMG. As in the original CGILS study [*Zhang et al.*, 2012], the vertical profiles of ozone are prescribed differently for each case to capture their meridional variation, whereas the default RRTMG concentrations are used for other greenhouse gases for all cases. Following *Blossey et al.* [2013], we estimate the cloud droplet effective radius r_{eff} needed in radiative transfer calculations from the volume-mean radius

$$r_v = \left(\frac{3 \rho_a q_l}{4 \pi \rho_l N_d} \right)^{1/3},$$ (1)

as

$$r_{eff} = r_v \exp \left[\log{(\sigma_g)}^2 \right],$$ (2)

where $\sigma_g = 1.2$ is the geometric standard deviation of an assumed lognormal droplet radius distribution [*Ackerman et al.*, 2009]. Other constants and variables appearing in these expressions are the density of air ρ_a, the density of liquid water ρ_l, and an assumed cloud droplet concentration $N_d = 100 \, \text{cm}^{-3}$.

Because the LES domain has limited height (about 4.3 km in our case), whereas radiative energy fluxes substantially interact with the atmosphere to much greater heights, the radiative transfer calculations need to be extended from the top of the LES domain to the top of the atmosphere (TOA). We do so by extending the reference profiles of temperature and specific humidity used for the large-scale forcings (to be discussed below) to TOA.

Radiative transfer is computed with RRTMG every 90 s. Radiative heating/cooling rates are computed and applied column-by-column within the LES domain. We have also experimented with horizontally homogenized radiative forcings, computed with horizontally averaged fields in the LES domain. However, the missing local radiative feedback affected the LES's ability to simulate the Sc-over-Cu case.

2.3. Surface Energy Balance

A mixed-layer (slab) ocean is coupled to the LES domain. Its temperature T_s evolves according to the surface energy balance:

$$(\rho_w C_w H_w) \frac{dT_s}{dt} = \text{RAD} - \text{OHU} - \text{SHF} - \text{LHF}.$$ (3)

Here $\rho_w = 10^3 \, \text{kg m}^{-3}$ is the density of ocean water, $C_w = 4.19 \times 10^3 \, \text{J kg}^{-1} \, \text{K}^{-1}$ is the specific heat capacity of water, and H_w is the depth of the slab ocean, which is chosen to be small ($H_w = 1 \, \text{m}$) to ensure fast equilibration of the model. The surface energy budget is balanced in the statistically steady state ($dT_s/dt = 0$). This steady state does not depend on the choice of H_w. The equilibration process does not accelerate significantly by further reducing H_w, since the moist heat capacity of the boundary layer is already comparable to 0.5–3 m of water. RAD is the net radiative flux into the surface, defined as

$$\text{RAD} = F_{SW}^{\downarrow} - F_{SW}^{\uparrow} + F_{LW}^{\downarrow} - F_{LW}^{\uparrow}.$$ (4)

These upward and downward longwave (LW) and shortwave (SW) radiative fluxes at the surface are obtained from RRTMG. SHF and LHF are the sensible and latent heat fluxes, computed with the bulk aerodynamic formulas and Monin-Obukhov similarity theory. SHF is obtained from the specific entropy and LHF flux as described in *Pressel et al.* [2015]. OHU is a prescribed parameter; it can be thought of as arising either from seasonal uptake of energy by the ocean or convergence of ocean energy transport.

In a forcing framework that resembles more traditional approaches such as the CGILS framework, the LES can also be coupled to an ocean surface with fixed SST. This corresponds to the limit $H_w \rightarrow \infty$ in the surface energy balance (3).

2.4. Microphysics

We use the Seifert-Beheng two-moment warm-rain microphysics scheme described in *Seifert and Beheng* [2001, 2006] and *Stevens and Seifert* [2008]. The distribution of raindrop diameters D is assumed to follow a generalized Γ distribution, with a shape parameter μ and a scale D_p. The probability density function of raindrop diameters is

$$f_r(D) = \frac{n_r}{D_p \Gamma(\mu+1)} \left(\frac{D}{D_p}\right)^\mu \exp\left(-\frac{D}{D_p}\right),$$ (5)

where n_r is the rainwater number density (per unit air mass). By integrating the distribution function, the rainwater specific humidity q_r can be shown to satisfy

$$q_r = \frac{\rho_l \pi}{6} n_r D_p^3 \frac{\Gamma(\mu+4)}{\Gamma(\mu+1)}.$$ (6)

Thus, D_p can be determined from n_r and q_r, assuming some closure for μ.

The microphysics scheme in PyCLES prognoses q_r and n_r, with source and sink terms representing various microphysical processes, and it diagnoses D_r and μ given n_r and q_r. The microphysical processes include the autoconversion from cloud liquid into rain droplets, accretion of cloud liquid onto existing rain droplets, self-collection of smaller rain droplets into larger ones, breakup of larger rain droplets into smaller ones, evaporation of rain into unsaturated air, and sedimentation of rain. The tendencies of q_r and n_r due to these processes are parameterized according to *Seifert and Beheng* [2006] with some recent updates: the breakup process, sedimentation velocity, and closure of μ are formulated as in *Stevens and Seifert* [2008]; the evaporation tendencies are formulated as in *Seifert* [2008]; the autoconversion coefficient is increased to represent the effects of turbulence, following *Heus et al.* [2010]. Additionally, the sedimentation of cloud droplets is formulated as in *Ackerman et al.* [2009], with the updated parameters (e.g., the lognormal distribution parameter $\sigma_g = 1.34$) as in *Heus et al.* [2010].

2.5. Large-Scale Forcings

Four large-scale forcing terms are included in the thermodynamic and water budgets: subsidence, relaxation toward a reference profile in the free troposphere, horizontal advection near the surface, and Coriolis accelerations owing to a prescribed geostrophic wind.

One major difference between the new framework and CGILS is the large-scale forcing in the free troposphere. The CGILS framework prescribes the horizontal advection tendency to exactly balance the radiative and subsidence tendencies above 800 hPa. It also formulates strong nudging above a prescribed nudging height, which is held fixed when forcing parameters are varied. This separation results in some redundancy and artificiality. The new framework unifies both tendencies into a relaxation term that represents the combined effects of large-scale horizontal fluxes and vertical eddy fluxes, and this relaxation is limited to the free troposphere above the model-simulated MBL. This adaptive configuration is able to provide realistic free-tropospheric forcing even when the MBL height changes significantly. Therefore, it is more suitable for simulating cloud regime transitions and climate change scenarios.

2.5.1. Subsidence
The subsidence tendencies are computed as

$$\left.\frac{d\phi}{dt}\right|_{sub} = -w_{ls}\frac{\partial\phi}{\partial z},$$ (7)

where ϕ stands for specific entropy (s) or total water specific humidity (q_t). The large-scale subsidence velocity profile w_{ls} is prescribed and time-independent. Subsidence of momentum components (u, v, w) is not implemented. Otherwise, the geostrophic wind would require modification to satisfy the balance between Coriolis accelerations and subsidence.

2.5.2. Relaxation Toward Reference Profile
In the free troposphere, specific entropy s and total water specific humidity q_t (and thus temperature and moisture) are relaxed toward prescribed reference profiles to represent the combined effects of large-scale horizontal fluxes and vertical eddy fluxes. In addition, the horizontal wind components u and v are relaxed toward the prescribed geostrophic wind to prevent drifts in the wind profile. The relaxation tendency is given by

$$\left.\frac{d\phi}{dt}\right|_{rel} = -\xi_r(z)(\phi-\phi_r).$$ (8)

Here ϕ stands for s, q_t, u, or v, and the reference profile ϕ_r is representative of the location under consideration. In the climate change experiments to be discussed in the companion paper, s_r and q_r are specified as

a tropical radiative-convective equilibrium (RCE) temperature profile with a given relative humidity. In this paper, because we are focusing on specific subtropical locations in the present climate, we use ϕ_r profiles that are close to observations (details in section 3.2), and $(u_r, v_r) = (u_g, v_g)$ is the geostrophic wind.

The relaxation coefficient $\xi_r(z)$ varies continuously with height from large values (strong relaxation) in the free troposphere to zero (no relaxation) in the boundary layer. Since the inversion height z_i may vary as large-scale conditions are varied, the profile of $\xi_r(z)$ is interactively determined based on the diagnosed z_i. For each time step, z_i is determined as the lowest level at which the horizontal mean of the total specific humidity, $\bar{q}_t$, is below a fixed multiple α of the reference value, i.e., the lowest level at which

$$\bar{q}_t(h) \leq \alpha q_{t,r}(z_i), \tag{9}$$

is satisfied. This formulation of determining z_i works well for subtropical cloud-topped boundary layers, in which the specific humidity jump is strong at the inversion. The value z_i is also insensitive to α as long as $1 < \alpha < 2$; we use $\alpha = 1.2$.

The profile of the relaxation coefficient $\xi_r(z)$ depends on z_i as follows, similar to the original CGILS study [*Blossey et al.*, 2013]

$$\xi_r(z) = \begin{cases} 0 & \text{for} \quad z/z_i < 1.2, \\ \frac{1}{2}\tau_r^{-1}\left[1 - \cos\left(\frac{z/z_i - 1.2}{1.5 - 1.2}\right)\right] & \text{for} \quad 1.2 \leq z/z_i \leq 1.5, \\ \tau_r^{-1} & \text{for} \quad z/z_i > 1.5. \end{cases} \tag{10}$$

Here $\tau_r = 24\,\text{h}$ is the relaxation time scale in the free troposphere.

As is common, the relaxation toward a reference profile is included to ensure that the free troposphere equilibrates to realistic conditions, without overly constraining features such as the boundary layer height by strongly relaxing toward reference profiles on which a boundary layer structure is already imprinted. Prescribing a subsidence velocity then becomes necessary to obtain a boundary layer height than can equilibrate at levels below those at which the relaxation time scale becomes fast compared with dynamical adjustment time scales.

Additionally, the mean specific humidity q_t at any level below 2000 m is nudged back to 20% of its saturated value on a time scale of 1 h, whenever it drops below this lower relative humidity limit. This nudging is similar to that used in *Blossey et al.* [2013]. It helps to reduce a q_t minimum just above the inversion that develops in the Sc simulations. This unrealistic feature arises from the mismatch between the prescribed vertical extent of horizontal advective drying and the actual boundary layer height.

2.5.3. Horizontal Advection
Because the relaxation forcing vanishes near the surface, large-scale fluxes near the surface need to be represented separately at lower levels. We do so by prescribing horizontal advective tendencies at levels below 800 hPa. Advective tendencies are assumed to be constant at levels below 900 hPa and linearly decrease to zero between 800 and 900 hPa

$$\left.\frac{d\phi}{dt}\right|_{\text{adv}} = \begin{cases} \dot{\phi}_s & \text{for} \quad p > 900\,\text{hPa}, \\ \dot{\phi}_s \times \dfrac{p - 800\,\text{hPa}}{900\,\text{hPa} - 800\,\text{hPa}} & \text{for} \quad 800\,\text{hPa} \leq p \leq 900\,\text{hPa}, \\ 0 & \text{for} \quad p < 800\,\text{hPa}. \end{cases} \tag{11}$$

Here ϕ stands for temperature T or total water specific humidity q_t. The tendency of specific entropy s is then calculated from the tendencies of T and q_t, as described in *Pressel et al.* [2015].

2.5.4. Coriolis Acceleration
Ageostrophic Coriolis accelerations are included in the horizontal momentum equations as

$$\left.\frac{du}{dt}\right|_{\text{cor}} = -f(v_g - v), \qquad \left.\frac{dv}{dt}\right|_{\text{cor}} = f(u_g - u), \tag{12}$$

where $f = 2\Omega\sin(\varphi)$ is the Coriolis parameter, which depends on planetary rotation rate Ω and latitude φ, and (u_g, v_g) is the prescribed geostrophic wind.

Table 2. Geographical Locations and Surface Energy Budgets of the Three Representative Low-Cloud Cases (S6, S11, and S12)[a]

Case Name	LAT (°)	LON (°)	SST (K)	SHF (W m^{-2})	LHF (W m^{-2})	RAD (W m^{-2})	OHU (W m^{-2})	I (W m^{-2})
S6 (Fixed-SST)	16.5	N/A	298.9	9.1	138.7	212.8	65.0	N/A
S6 (ERA-I)	16.5	−148.5	298.9	10.3	141.6	210.0	58.1	N/A
GPCI (KLT)	*15–20*			*11*	*145*			
S6 (CGILS)	17	−149	298.8	10.1±2.0	118.6±4.7	220±6	91±6	447.9
S11 (fixed-SST)	31.5	N/A	292.2	2.6	91.0	182.8	89.2	N/A
S11 (ERA-I)	31.5	−129.0	292.2	14.9	85.6	207.4	107.0	N/A
GPCI (KLT)	*30–35*			*15*	*81*			
S11 (CGILS)	32	−129	292.5	4.3±0.5	97.8±2.6	139±17	37±17	470.3
S12 (fixed-SST)	34.5	N/A	289.8	0.8	85.5	157.3	71.0	N/A
S12 (ERA-I)	34.5	−124.5	289.8	10.9	61.3	230.7	158.5	N/A
S12 (CGILS)	35	−125	291.0	3.9±2.4	82.3±3.6	157±19	71±19	471.6

[a]The data sources are days 11–15 average of the fixed-SST simulations (fixed-SST), ERA-Interim mean July climatology (ERA-I), GPCI MBL budget analysis by *Kalmus et al.* [2014] (KLT), and the CGILS LES intercomparison (CGILS). The data columns are latitude (LAT) and longitude (LON), SST, sensible heat flux (SHF), latent heat flux (LHF), net radiative energy gain (RAD), and OHU required for surface energy balance (diagnosed as the residual of other terms). The CGILS results are reported with the standard deviation across all available models. Insolation values (i.e., top-of-atmosphere downward SW radiation) from CGILS cases are also listed (I).

3. Representative Subtropical MBL Regimes

We test the forcing framework for the three locations along the GCSS Pacific Cross-Section Intercomparison (GPCI) region [*Teixeira et al.*, 2011] considered in CGILS [*Blossey et al.*, 2013], which represent prototypical regimes of subtropical MBL clouds: Sc (S12, 34.5°N, 124.5°W), transitional Sc over Cu (S11, 31.5°N, 129.0°W), and Cu (S6, 16.5°N, 148.5°W). The free-tropospheric reference profiles ϕ_r and the target SST at steady states for each location are derived from the climatological average July conditions over the years 1979–2012 from ERA Interim reanalysis [*Dee et al.*, 2011]. They differ only slightly from the mean conditions for July 2003 that were used in CGILS.

3.1. Ocean Energy Uptake

To determine OHU in the surface energy balance (3), a set of three fixed-SST LES experiments is run to a statistically steady state for diagnostic purposes. These experiments are configured and forced in exactly the same way as the control experiments with prescribed OHU, except that their SST are prescribed and fixed at values diagnosed from the ERA Interim reanalysis. The averaged surface energy budgets for days 11–15 are shown in Table 2, in comparison with the corresponding results from reanalysis and from MBL budget analysis by *Kalmus et al.* [2014]. OHU diagnosed from the fixed-SST simulations is similar to the corresponding reanalysis energy uptakes for the S6 and S11 cases. For the S12 case, the SW cloud radiative effect (SWCRE) may be underestimated in the reanalysis, since Sc cover is likely biased low in the reanalysis [*Teixeira et al.*, 2011]. Therefore, the net surface heating by radiation may be overestimated, and the compensating OHU is likely biased high in the reanalysis. The lower OHU diagnosed from PyCLES is consistent with the strong SWCRE of the Sc regime and may be more realistic.

The fixed-SST surface energy budgets are further compared with the CGILS LES results (Table 2). The CGILS SHF and LHF data are computed from the mean of all LES model results in *Blossey et al.* [2013, Tables 3–5]. An off-line RRTMG calculation is run with CGILS reference profiles of temperature and moisture and a cloud layer (Sc layer for the S11 and S12 cases, and Cu layer with uniform 10% cloud fraction for the S6 case), where the liquid water content was assumed to increase linearly between the cloud base height z_b and the cloud top height z_i, and the liquid water path (LWP) was set to match the reported CGILS values. The surface net radiative fluxes (RAD) are then estimated as the sum of RRTMG cloudy net surface LW flux and the clear-sky net surface SW flux, offset by the reported TOA SWCRE that was scaled by a factor of 1.1 to obtain surface SWCRE values. (The net surface flux produced directly by off-line RRTMG calculations is significantly biased, possibly because of the lack of spatial variations in cloud liquid water; we do not use it.) The required OHU (cooling) is then diagnosed on the basis of the surface energy balance assuming that SST is stationary, i.e., right-hand side of the surface energy balance (3) is zero.

The CGILS S12 surface energy budget is similar to our fixed-SST results. The Sc layer in the CGILS S11 case is thicker and more opaque, consistent with its enhanced SWCRE and weakened SW heating at sea surface, compensated by its reduced OHU. The spread of net surface radiative fluxes among different CGILS LES

models is significant (30–40 W m^{-2}) for the S11 and S12 cases, and thus the estimated OHU would also differ by as much. For the S6 case, the CGILS OHU is much higher, because of the prescribed advective moistening above 1500 m altitude that moistens the boundary layer and reduces the surface LHF.

On the basis of our fixed-SST results, the OHU for the control experiments is prescribed to be 60 W m^{-2} for the S6 case, 90 W m^{-2} for the S11 case, and 70 W m^{-2} for the S12 case. As shown in Table 2, these values are roughly consistent with the ERA Interim reanalysis and CGILS LES results, with differences attributed to the differences in the simulated LWP and SWCRE, and to the differences in the prescribed advective forcing for the S6 case. Sensitivities to perturbations in OHU are further discussed in section 5.

3.2. Large-Scale Forcings

The potential temperature θ and relative humidity (RH) profiles from the ERA Interim climatology and from CGILS are compared in Figures 1a and 1b. The θ and RH profiles are very similar between ERA Interim and CGILS. However, the CGILS boundary layer is slightly shallower in the S11 and S12 cases, so the free-tropospheric air just above the boundary layer top is warmer and drier. The free-tropospheric θ profiles are very similar between the S6, S11, and S12 cases, reflecting the weak temperature gradient (WTG) constraint in the tropics.

The free-tropospheric θ profiles are all close to the moist adiabat initialized from a saturated parcel at $p = 1000$ hPa and $T = 295$ K. Therefore, this adiabat is used as the reference temperature profile in our study. The free-tropospheric RH is around 25% for all cases, and the reference RH profile is set to be slightly higher to 30% to compensate for the subsidence drying. The reference profiles of specific entropy s and total water specific humidity q_t are computed accordingly. The reference profiles of s and q_t are defined throughout the atmospheric column, but they are only important in the free troposphere, where relaxation is significant.

The large-scale subsidence profiles in pressure coordinates (with vertical velocity $\omega = dp/dt$) are compared in Figure 1c. The CGILS subsidence is stronger than the climatology for the S11 and S12 cases, consistent with the shallower boundary layers inferred from the θ and RH profiles. We prescribe the large-scale subsidence profiles as

$$w_{ls} = -\frac{\omega}{\rho_0 g} \qquad \text{with} \qquad \omega = -D(p_0 - p_s)(p_0/p_s)^2, \qquad (13)$$

where ρ_0 and p_0 are the anelastic basic-state profiles of density and pressure. This formulation satisfies $\partial\omega/\partial p = -D$ at the surface ($p_0 = p_s$), i.e., the surface-layer divergence rate is D. It also satisfies $\omega = 0$ when $p_0 = p_s$ or $p_0 = 0$. For the S6, S11, and S12 cases, D is taken to be 2.0×10^{-6} s^{-1}, 3.5×10^{-6} s^{-1}, and 6.0×10^{-6} s^{-1}, respectively. The resultant ω profiles are also shown in Figure 1c; they are roughly consistent with the corresponding CGILS ω profiles. The S12 ω profile from the reanalysis is about 20% weaker than our prescribed value and the CGILS value. We have verified (section 5) that the steady state associated with the reduced ω is a deeper and weakly decoupled Sc-layer. In contrast, the chosen ω profile results in a well-mixed Sc regime, which is more representative of the coastal MBL.

The geostrophic wind speed profiles are compared in Figure 1d. The S11 and S12 wind speeds decrease strongly with height, consistent with the westerly thermal wind shear the edge of the Hadley cell. The S6 wind speed also decreases with height, albeit less strongly. In the current study, the prescribed geostrophic wind profile is chosen to be linearly decreasing from 10 m s^{-1} at the surface to 5 m s^{-1} at $p_0 \approx 600$ hPa, and its direction does not change with height. This wind profile is used for all three cases; it is similar to horizontal winds in ERA Interim reanalysis and CGILS.

Boundary layer horizontal advective tendencies are prescribed to be $\dot{T} = -1.2$ K d^{-1} and $\dot{q}_t = -0.6 \times 10^{-3}$ d^{-1}. The advective tendencies are the same for all three cases. These values are similar to the CGILS boundary layer advective tendencies, except that CGILS prescribes significant advective moistening above 1500 m for the S6 cumulus case, which cancels most of the advective drying [*Zhang et al.*, 2013]. Sensitivities to perturbations in these large-scale forcings are further discussed in section 5.

3.3. Experimental Setup

The simulations are run on a uniform grid, with horizontal resolution $\Delta x = \Delta y = 75$ m and vertical resolution $\Delta z = 20$ m. The domain sizes are horizontally $L_x = L_y = 6400$ m and vertically $L_z = 4320$ m. The simulations are
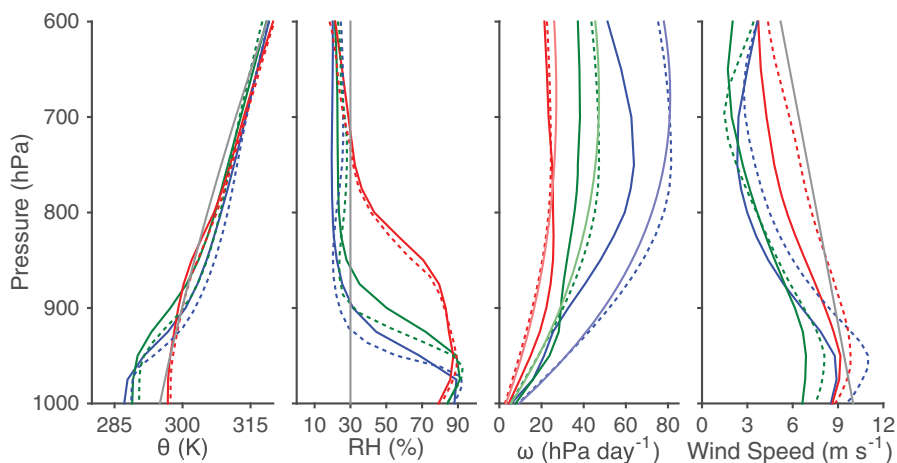
Figure 1. Prescribed reference profiles (gray or light colored solid lines) of potential temperature (θ), relative humidity (RH), subsidence (ω), and geostrophic wind speed. ERA-Interim mean July climatology profiles (years 1979–2012, solid lines) and the reference profiles prescribed for CGILS LES experiments (dashed lines) are shown for comparison. Different colors represent the S12 (Sc, blue), S11 (Sc-over-Cu, green), and S6 (Cu, red) cases.

run for 24 simulated days. For each of the S6, S11, and S12 cases, simulations are run both with fixed SST and with fixed OHU. The simulations are run with the RRTMG radiation scheme with the same TOA insolation without diurnal cycle as in CGILS, and with the Seifert-Beheng warm-rain microphysics scheme.

The results are not qualitatively sensitive to the horizontal resolution (Δx and Δy). However, the S11 and S6 cases are somewhat sensitive to the domain size (L_x and L_y): With the same prescribed OHU, smaller domains tend to have cloudier and cooler boundary layers, and vice versa. The S11 case in larger domains warms up and transitions to a Cu regime. The S6 case is not sensitive to vertical resolution (Δz), but the S11 and S12 Sc-layers are only simulated reliably when $\Delta z \lesssim 25$ m; however, LWP continues to increase as Δz is further reduced. This is consistent with *Blossey et al.* [2013], who suggested using $\Delta z = 5$ m for S11 and S12. LWP also increases significantly if the SGS diffusion is disabled above the surface layer (K. G. Pressel et al., submitted, 2016). This sensitivity is further discussed in Appendix A.

4. Control Experiment Results

For experiments both with fixed SST and with fixed OHU, the initial θ and RH profiles are the same as the reference profiles above 920 hPa, and the initial profiles below 920 hPa are set to be a vertically well-mixed layer with homogenized θ_l and q_t, calculated from the surface air temperature $T_a = 288$ K and RH = 80%. Therefore, a cloud deck sits between 950 and 920 hPa initially. The initial wind profile is the same as the prescribed geostrophic wind. The surface pressure is $p_s = 1018$ hPa for all cases.

The SST in the fixed-OHU cases are initialized with the same values as in the fixed-SST cases. Because the initial boundary layer profiles are in disequilibrium with the SST and are far from a quasi steady state, the surface heat fluxes are initially very large. Consequently, the surface energy budget is strongly out of equilibrium during spin-up, causing the SST to drift. To avoid such drift, SST in fixed-OHU cases is kept fixed for 3 days, before it can evolve freely according to the surface energy balance.

Figure 2 shows the time-height profiles of 6 h mean cloud fraction from both sets of simulations, and Figure 3 shows the evolution of 24 h mean LWP, SST, and the surface energy gain (SEG), defined as: SEG=RAD−SHF−LHF. According to the surface energy balance (3), the SST of the interactive slab ocean is steady if SEG=OHU.

Similar to the CGILS study, all three fixed-SST cases reach a statistically near-steady state by days 7–10. The fixed-OHU cases reach slowly evolving quasi steady states by day 10, and SST drifts are smaller than 0.4 K from day 10 to day 20. However, fully steady state takes much longer to establish. Due to computational constraints, we have opted to focus on the quasi steady results for days 11–15.
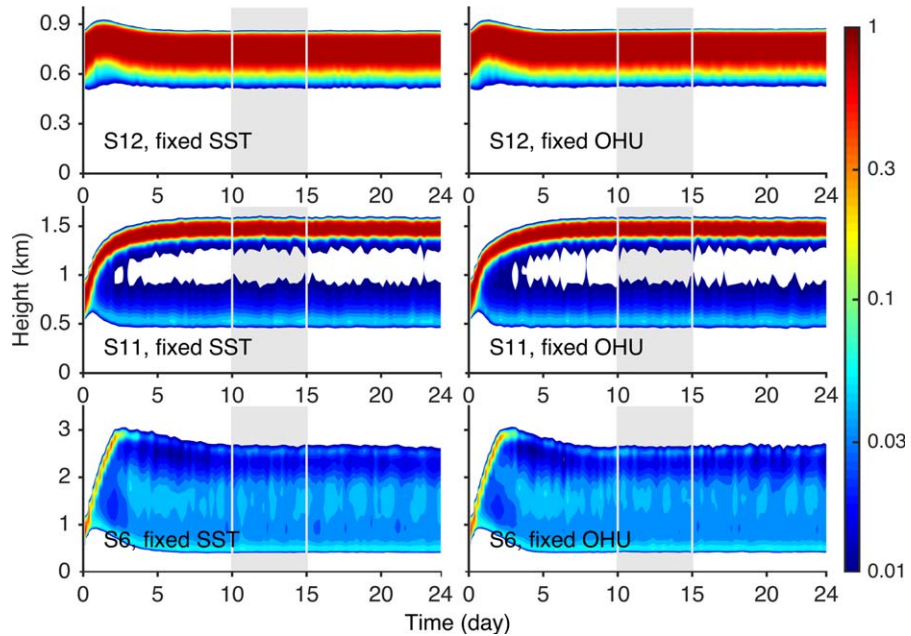
Figure 2. Evolution of 6 h mean cloud fractions from the control experiments with fixed SST (left column) and with fixed OHU (right column).

Both sets of experiments agree very well in their quasi steady state cloud profiles (Figure 2), as well as in LWP, SST, and surface energy budgets (Figure 3). This agreement relies on choosing OHU of the fixed-OHU cases to be near that implied by the fixed-SST cases. The S12 case maintains a Sc layer between altitudes of 500 m and 800 m, with cloud cover near 100% and LWP $\approx$ 47 g m^{-2}. The S11 case grows from the Sc initial condition into the Sc-over-Cu regime, with Cu cloud bottom at 450 m and an Sc layer between 1350 and 1550 m. The cloud cover is about 97% and LWP $\approx$ 26 g m^{-2}. The S6 case grows into a Cu layer extending from 400 to 2600 m altitude, with cloud cover about 24% and LWP $\approx$ 35 g m^{-2}. The S6 fixed-OHU case maintains a slightly lower SEG compared to the fixed-SST case, because slightly higher LHF and SHF are required to fuel the continuous warming of its evolving boundary layer. Fluctuations of cloud fraction, LWP and SEG remain evident (Figures 2 and 3) in the quasi steady states, as a result of the life cycles of the sample of turbulent eddies and clouds in the limited domain.

The mean profiles of θ, RH, q_l and cloud fraction averaged over days 11–15 are shown in Figure 4, and they are almost the same for both sets of experiments.

4.1. Comparison of Results Under New and CGILS Frameworks
An additional set of three simulations are run with the same large-scale forcing as in the CGILS simulations [*Blossey et al.*, 2013], but with a different Δz: $\Delta z = 30$, 20, and 12 m, respectively, for the S6, S11, and S12
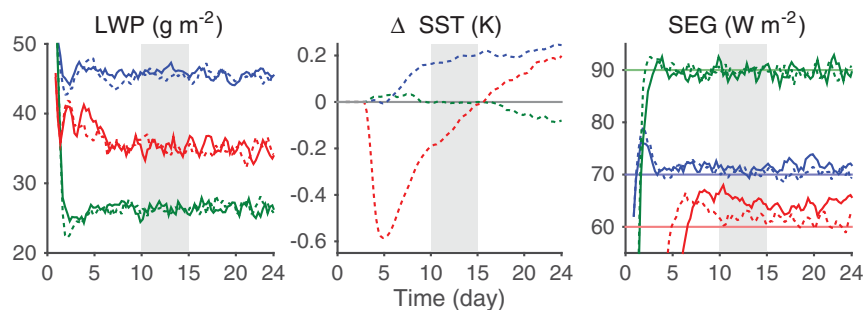

Figure 3. Time series of 24 h mean LWP, SST, and SEG from the control experiments with fixed SST (solid) and with fixed OHU (dashed). The surface energy gain is positive for energy flux into the surface. In a steady state in the fixed-OHU experiments, SEG is equal to the prescribed OHU (light colors). Colors as in Figure 1.

cases. The quasi steady mean profiles are shown in Figure 4 (light colors). They are similar to the LES mean results in *Blossey et al.* [2013], except that the LWP of the S11 and S12 cases are lower by ∼50 and ∼30%, respectively, possibly because of the coarser vertical resolution of our simulations.

For the S6 cases, the θ_l and q_t profiles, inversion depth, and Cu fraction are very similar under the original CGILS and the new framework. However, the simulation under the new framework has much stronger buoyancy production in the Cu layer, which almost doubles $\overline{w'^2}$. The increased in-cloud buoyancy production is consistent with the enhanced surface LHF (cf. Table 2) under the new framework, which compensates for the elimination of the prescribed moistening above 1500 m in CGILS. The Cu updrafts are thus more energetic, less diluted, and richer in q_l. As a result, the domain-mean LWP is 9 g m^{-2} higher, and the surface precipitation rate is also slightly higher (1.0 mm d^{-1} under the new framework, compared to 0.9 mm d^{-1} under the CGILS framework).

The S11 case under the new framework produces a slightly deeper boundary layer compared to the CGILS framework, consistent with its weaker advective cooling and drying in the boundary layer. The surface buoyancy flux is also weaker, mainly due to the reduction of SHF. The buoyancy production of turbulence in the subcloud layer is correspondingly weaker, so that $\overline{w'^2}$ is reduced, and the bottom of the Cu layer is lower. The Sc layer below the inversion has lower q_l than under the CGILS framework, possibly related to the lower q_t in the free troposphere and the slightly stronger inversion strength. As discussed in section 3.3, the larger domain size (L_x=6.4 km instead of 4.8 km) and rougher horizontal resolution (Δx=75 m instead of 50 m) of the new S11 case also tend to reduce LWP. The surface precipitation is negligible (<0.002 mm d^{-1}) under both frameworks.

The Sc layer in the S12 case under the new framework is also slightly deeper and less vertically coupled, as seen from the $\overline{w'^2}$ profile, consistent with its slightly weaker SHF and stronger LHF. The Sc layer is about 50 m deeper, and LWP is about 60% higher. Since the prescribed subsidence profiles and advective tendencies are almost the same under both frameworks, the deeper and moister Sc layer under the new framework may be related to its 1 K cooler SST and a 2 K cooler free troposphere, which in combination lead to slight reductions in the inversion strength and inversion moisture jump. However, the higher LWP is accompanied by weaker subcloud turbulence (smaller $\overline{w'^2}$), which can be attributed to the much rougher resolution (Δx=75 m instead of 25 m; Δz=20 m instead of 12 m) of the new S12 case. The precipitation is negligible (<10^{-4} mm d^{-1}) under both frameworks.

In summary, the new framework of large-scale forcing is capable of reproducing the qualitative features of all three low-cloud regimes (S6 Cu, S11 Sc-over-Cu, and S12 Sc) considered in the CGILS study. The differences in forcing, model domain size, and resolution lead to some quantitative differences, such as a Cu layer that is more energetic and liquid-rich in the S6 case, subcloud layer turbulence that is weaker, and an inversion that is slightly higher in the S11 and S12 cases. These differences should not affect interpretation of cloud feedback mechanisms under climate change.

5. Sensitivity to Perturbations in Forcing

For each of the S6, S11, and S12 cases with fixed OHU, a set of six tests are run to investigate the sensitivities to perturbations in large-scale subsidence (±25%, denoted as Sub±), horizontal advective cooling and drying (±25%, denoted as Adv±), and OHU (±20 W m^{-2}, denoted as OHU±). A corresponding set of fixed-SST tests (Sub±, Adv±, and Ctl) are run for comparison. All simulations are restarted from the day 11–15 mean vertical profiles (not the full 3-D field) of the control experiments and run for 15 days. For the fixed-OHU cases, the SST is fixed for the first day of simulation while turbulence spins up. An unperturbed baseline simulation is also run (denoted as Ctl), as a continuation of the simulations described above, to be able to separate effects of lack of stationarity from perturbation effects.

The average conditions for day 13–15 are presented in Tables 3–5. The column IMBAL=SEG−OHU is the right-hand side of the surface energy balance (3). For the fixed-OHU cases, a positive IMBAL causes SST to rise, and vice versa. Therefore, IMBAL indicates how far away the fixed-OHU results are from a steady state. For the fixed-SST cases, IMBAL is usually much greater, since the surface acts as an infinite heat bath that can sustain much larger SHF and LHF responses to perturbed forcing.
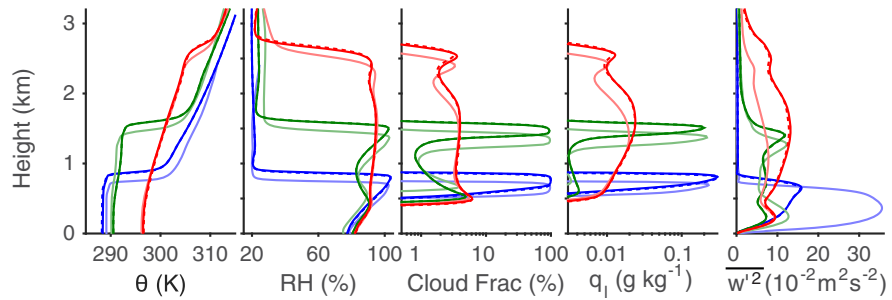
Figure 4. Steady state profiles of potential temperature (θ), relative humidity (RH), cloud fraction, liquid water specific humidity (q_l), and resolved variance of vertical velocity ($\overline{w'^2}$). Solid and dashed lines are day 10–15 mean profiles from the control experiments with fixed OHU and with fixed SST, respectively. Mean profiles from PyCLES simulations with original CGILS forcing are shown in light colors. Colors as in Figure 1.

All fixed-OHU Ctl cases reach quasi steady states by day 15 with IMBAL $<1\,\text{W}\,\text{m}^{-2}$. Their SST are all very close to the prescribed values for the fixed-SST experiments. In contrast, most perturbed cases are still evolving with significant IMBAL. However, since IMBAL and SST changes have the same sign for all cases, we can infer that the evolution is monotonic, and thus the transient results are already representative of the perturbation effects. Almost all fixed-SST cases are in steady states by days 13–15. The only exception is the S12 Sub+ case, whose boundary layer continues to shallow and clear up, eventually reaching a cloud-free steady state by day 18.

The S6 Cu layer consists of three parts (Figure 5): (1) the bottom layer (bot-Cu) just above the lifted condensation level (LCL), which is passively driven by subcloud turbulence and where q_l is low; (2) the top layer (top-Cu) just below the inversion, which originates because cumulus updrafts detrain into stable stratification; (3) the middle Cu-layer (mid-Cu), which arises as buoyant saturated updrafts penetrate through a conditionally unstable environment that is shaped by the moistening and cooling effects of rain evaporation. Correspondingly, the S6 $\overline{w'^2}$ profile has three peaks, representing subcloud layer turbulence driven by surface buoyancy fluxes, cumulus layer turbulence driven by in-cloud latent heat release, and cloud top turbulence driven by radiative cooling.

The S11 cloud layer (Figure 6) usually consists of an upper Sc-layer (analogous to the S6 top-Cu layer but with much higher cloud fraction and q_l), and an underlying Cu-layer (similar to the S6 bottom layer) with cloud bottom at 450 m. Its $\overline{w'^2}$ profile also has two peaks, representing surface-driven and cloud top turbulence. The Sc-layer breaks up under Sub+, as well as Adv– and OHU– with fixed OHU.

Most of the S12 cases (Figure 7) are pure Sc, but the Sub– case evolves into Sc-over-Cu like S11, and the Sub+ case evolves into a shallow Cu-layer. The $\overline{w'^2}$ profile of the pure Sc layer shows only one broad peak of turbulence, which is driven by cloud top cooling augmented by surface fluxes.

Table 3. Mean Conditions of the S6 Unperturbed Test and Anomalies of the S6 Perturbed Tests[a]

CASE	SST	IMBAL	SHF	LHF	RAD	OHU	ZINV	INVS	LWP	CC	SWCRE	PREC
Ctl	298.9	0.8	9.2	142.3	212.2	60	2752	7.1	35.6	24.7	−34.6	1.1
	298.9	*3.5*	*9.0*	*139.9*	*212.5*	*60*	*2793*	*6.8*	*35.5*	*24.7*	*−34.6*	*1.1*
Sub+	−0.3	−1.1	−0.7	+1.7	−0.1		−261	+1.2	−4.8	+2.0	+0.8	−0.4
		−7.6	*−0.4*	*+8.6*	*+0.6*		*−223*	*+0.9*	*−3.7*	*−0.1*	*+1.9*	*−0.3*
Sub−	+0.2	+2.0	+0.4	−4.0	−1.6		+776	−1.4	+4.6	+2.0	−3.1	+0.3
		+6.1	*−0.1*	*−7.4*	*−1.4*		*+785*	*−1.0*	*+4.6*	*+2.0*	*−2.9*	*+0.2*
Adv+	−0.9	−2.2	+1.1	−4.1	−5.2		−138	+0.9	+1.3	+5.9	−5.1	−0.0
		−12.6	*+2.0*	*+8.7*	*−2.0*		*−5*	*+0.1*	*+1.8*	*+1.0*	*−1.4*	*+0.0*
Adv−	+0.7	+2.4	−1.3	+2.8	+3.9		+194	−0.9	−1.2	−2.8	+3.2	+0.0
		+13.2	*−2.1*	*−8.5*	*+2.6*		*−7*	*−0.0*	*−2.2*	*−1.5*	*+2.1*	*−0.1*
OHU+	−1.3	−3.2	−1.1	−18.2	−2.4	+20	−215	+1.0	−2.2	+4.3	−2.5	−0.2
OHU−	+1.1	+2.3	+0.8	+18.4	+1.5	−20	+273	−1.2	+2.2	−1.9	+1.1	+0.2

[a]Prescribed ocean heat uptake results are shown in roman font, and fixed-SST results are shown in italic font. Results are averaged for days 13–15. The naming of perturbation experiments follows section 5. SST and surface energy budget terms (SHF, LHF, RAD, OHU) are the same as in Table 2, and the surface energy imbalance (IMBAL) is diagnosed as the residual. Other terms are inversion height (ZINV, in m, defined as in equation (9)), inversion strength (INVS, in K, defined as $\Delta\theta$ between ZINV $\pm$ 250 m), liquid water path (LWP, in $\text{g}\,\text{m}^{-2}$), total cloud cover (CC, in %), surface SWCRE (in $\text{W}\,\text{m}^{-2}$), and surface precipitation rate (PREC, in $\text{mm}\,\text{d}^{-1}$).

Table 4. Same as Table 3, but for the S11 Tests

CASE	SST	IMBAL	SHF	LHF	RAD	OHU	ZINV	INVS	LWP	CC	SWCRE
Ctl	292.2	−0.4	2.4	91.6	183.7	90	1609	14.5	26.1	97.5	−106.3
	292.4	*−2.3*	*2.4*	*92.7*	*182.8*	*90*	*1650*	*14.2*	*26.3*	*97.9*	*−107.2*
Sub+	+2.7	+6.5	+4.5	+28.5	+39.5		−400	−4.0	−14.5	−63.7	+73.3
	+41.3	*+2.5*	*−5.6*	*+38.2*			*−660*	*−3.3*	*−14.9*	*−54.5*	*+67.5*
Sub−	−0.6	−1.4	+0.0	−12.2	−13.6		+421	+0.7	+5.7	+2.2	−15.6
	−0.5	*+0.2*	*−7.7*	*−8.0*			*+498*	*+0.4*	*+3.3*	*+1.6*	*−7.0*
Adv+	−2.5	−11.6	+0.1	−15.8	−27.4		−159	+1.4	+16.1	+2.4	−38.7
	−21.0	*+1.2*	*+8.2*	*−11.7*			*+97*	*+0.5*	*+6.3*	*+1.2*	*−14.1*
Adv−	+2.8	+9.4	+2.3	+21.5	+33.2		+17	−3.0	−9.9	−45.2	+59.7
	+30.6	*−0.1*	*−9.2*	*+21.4*			*−171*	*−1.1*	*−8.6*	*−12.0*	*+32.6*
OHU+	−2.5	−11.6	−1.2	−23.3	−16.1	+20	−219	+1.0	+9.3	+2.1	−26.5
OHU−	+2.4	+10.1	+2.7	+28.4	+21.3	−20	+167	−1.8	−6.0	−21.5	+40.3

A few general insights about the responses of the MBL properties (inversion height and strength) and cloud characteristics (cloud fraction, LWP, and SWCRE) to perturbations can be inferred from these results. They are summarized in a schematic (Figure 8), and the main pathways are discussed in what follows.

5.1. SST Changes Align With Perturbation in Energy Budget and SWCRE Feedback

The forcing perturbations provide additional energy sources or sinks of ±10–$20\,\mathrm{W\,m^{-2}}$ to the coupled system of the boundary layer and the slab ocean. For the fixed-OHU cases, when SWCRE feedback is weak (e.g., S6 Cu), cases with increased energy sinks (OHU+, Adv+, and Sub+) generally produce lower SST, cooler MBL, and thus increased inversion strength (see Table 3 and Figure 5). The negatively perturbed energy budget is rebalanced by the increased entrainment warming and decreased entrainment drying. The cases with opposite perturbations (OHU−, Adv−, and Sub−) generally produce reversed responses.

However, SWCRE feedback for Sc cases may exceed the imposed energetic perturbations, causing larger changes in SST (see Tables 4 and 5). It may even reverse the SST change due to the imposed perturbation (e.g., S11 Sub± and S12 Sub+). The magnitude of the SST change increases with the total energetic perturbation, including the SWCRE feedback (i.e., combination of all dashed arrows in Figure 8).

In contrast, if SST is fixed, the MBL temperature is strongly constrained and stays almost unchanged under perturbations. The MBL energy budget is mostly rebalanced by the changes in surface energy fluxes, mainly by LHF. This is very different from the LHF response in the fixed-OHU cases, discussed next.

5.2. LHF Change Balances OHU and SWCRE Perturbation

For the fixed-OHU cases, LHF changes are constrained by the surface energy budget. LHF increases in response to decreases in SWCRE cooling (Sub+, Adv−, and S12 Sub−) and ocean heat uptake (OHU−), and vice versa. SHF changes are generally much weaker and usually oppose changes in LHF, except for the OHU± cases and the cases with significant SWCRE reduction (S11 Sub+/Adv− and S12 Sub± cases, in which Sc transitions into Cu).

In contrast, LHF under fixed SST responds to counteract the MBL energetic perturbations and is unaffected by SWCRE. This LHF response can be opposite to that with fixed OHU (e.g., Adv±). Hence, caution must be

Table 5. Same as Table 3, but for the S12 Tests

| CASE	SST	IMBAL	SHF	LHF	RAD	OHU	ZINV	INVS	LWP	CC	SWCRE
Ctl	289.8	−0.6	0.6	85.5	155.5	70	870	14.2	47.7	99.8	−154.6
	289.8	*2.2*	*0.6*	*86.3*	*159.1*	*70*	*890*	*14.0*	*44.7*	*99.7*	*−149.7*
Sub+	+6.9	+6.5	+9.2	+56.8	+72.5		−177	−6.4	−43.3	−76.2	+133.3
	+73.0	*+7.3*	*−21.1*	*+59.2*			*−380*	*−1.8*	*−33.6*	*−23.8*	*+85.5*
Sub−	+2.3	+19.1	+4.0	+18.4	+41.4		+338	−0.8	−26.3	−14.2	+68.9
	+8.5	*+0.8*	*−6.6*	*+2.7*			*+240*	*+0.6*	*−3.9*	*−0.1*	*+7.6*
Adv+	−1.2	−2.7	+2.1	−6.1	−6.6		−63	+0.5	+4.9	+0.1	−8.9
	−10.3	*+1.5*	*+6.1*	*−2.7*			*+20*	*+0.1*	*+1.3*	*+0.0*	*−2.2*
Adv−	+1.2	+5.3	−1.2	+5.9	+10.1		+42	−0.6	−6.8	−0.9	+14.2
	+8.0	*−1.4*	*−6.0*	*+0.6*			*−20*	*−0.1*	*+0.2*	*+0.0*	*−0.3*
OHU+	−2.5	−4.7	+2.2	−24.1	−6.5	+20	−175	+0.8	+6.2	+0.2	−12.1
OHU−	+3.2	+31.5	+4.3	+28.8	+44.6	−20	+80	−2.0	−26.2	−34.1	+78.9
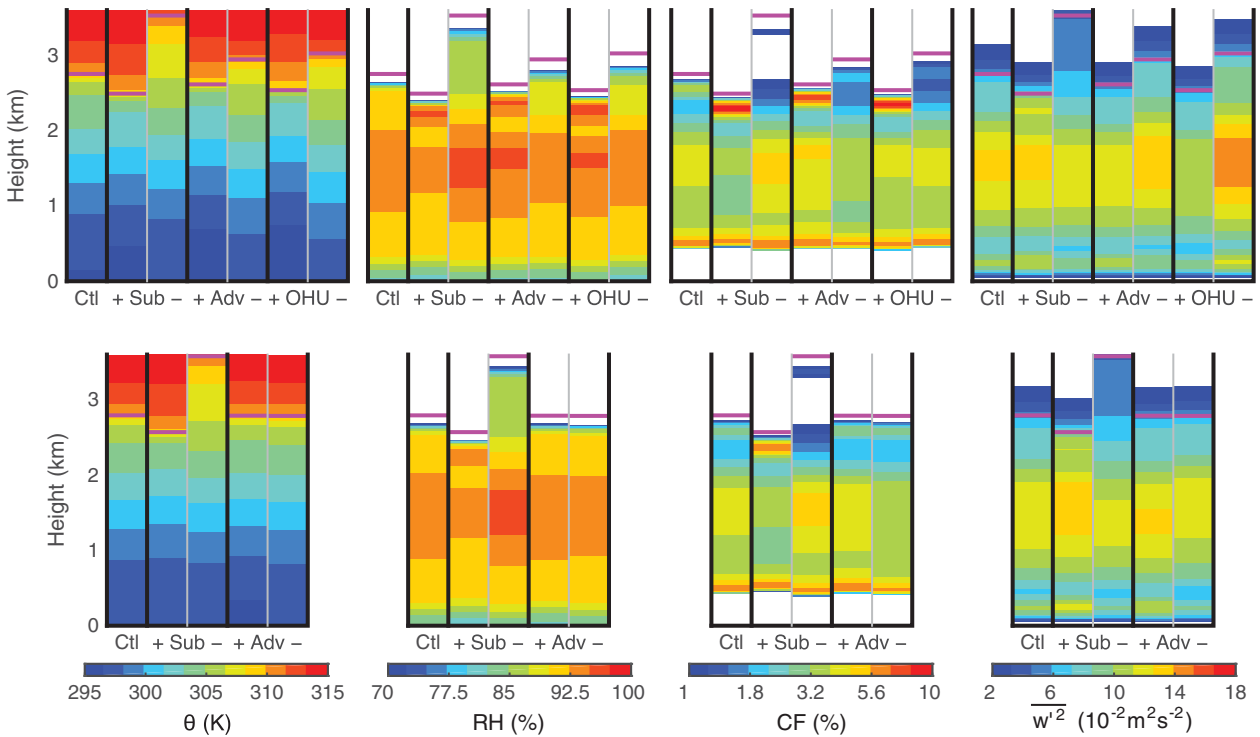
Figure 5. Mean vertical profiles of potential temperature (θ), relative humidity (RH), cloud fraction (CF), and resolved variance of w, for all S6 sensitivity tests. Top row: fixed OHU. Bottom row: fixed SST. Results are averaged between days 13 and 15. The solid magenta lines represent the inversion heights.
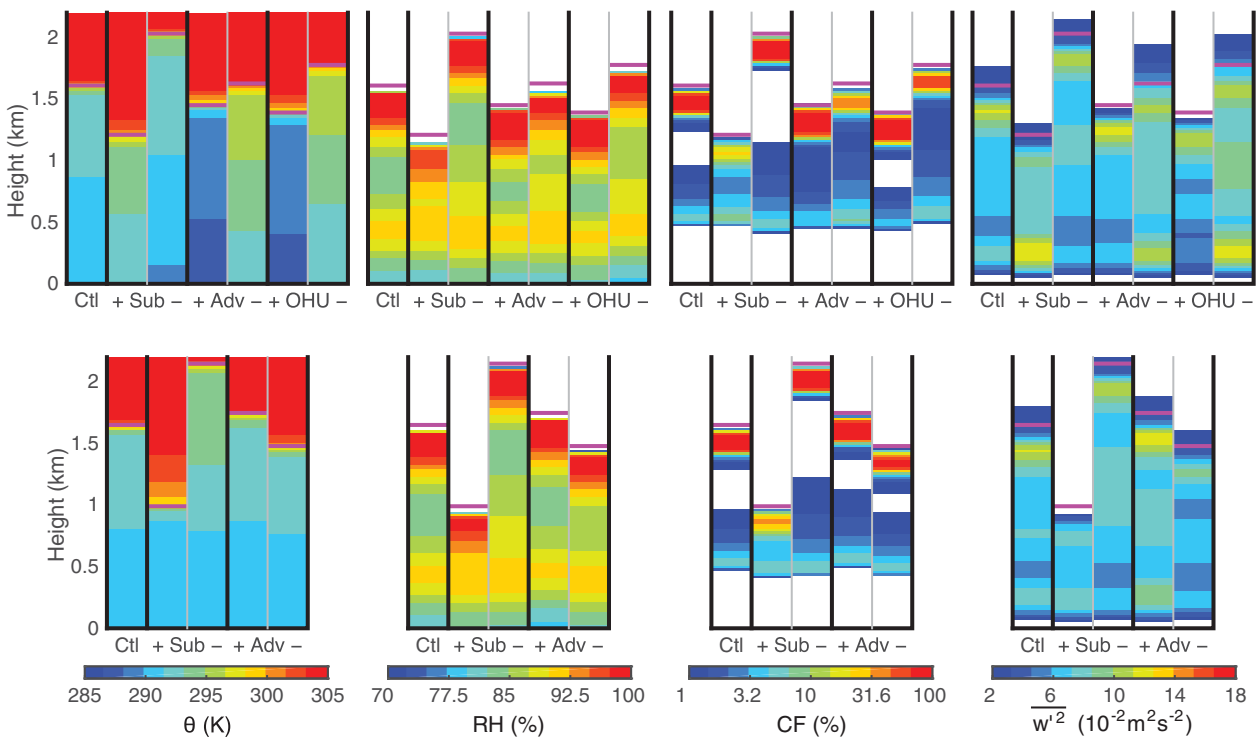

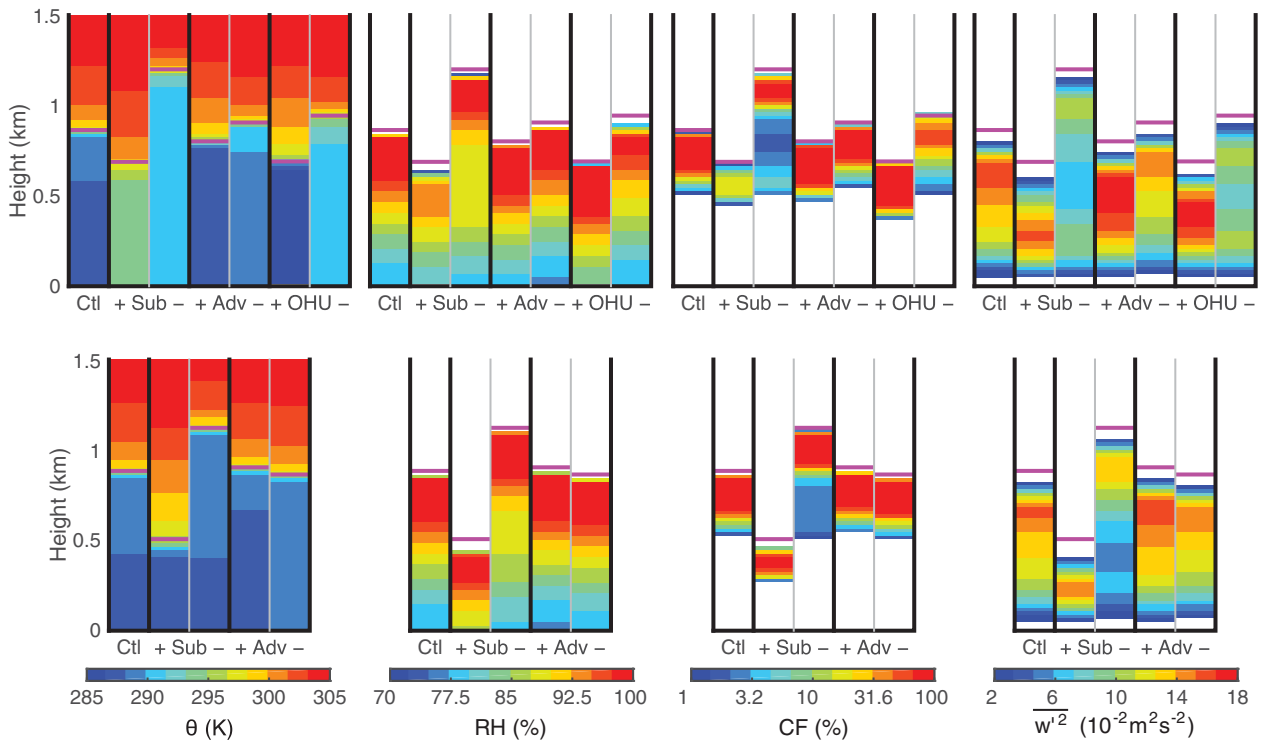**Figure 6.** Same as Figure 5, except for the S11 sensitivity tests.

Figure 7. Same as Figure 5, except for the S12 sensitivity tests.

exercised when trying to infer mechanisms of cloud responses to large-scale perturbations. The dominant mechanisms can differ substantially under a fixed-SST scenario and under the more realizable fixed-OHU scenario.

5.3. Inversion Height Increases as Subsidence Weakens or SST Rises

The inversion height z_i is highly sensitive to perturbations in large-scale subsidence (Sub$\pm$). With weakened subsidence (Sub$-$), entrainment exceeds subsidence and causes z_i to rise. This continues until the subsidence rate strengthens sufficiently to rebalance with entrainment (note that w_{sub} increases with height). The converse holds for strengthened subsidence (Sub$+$). This response applies across all regimes for both fixed-SST and fixed-OHU cases (Figures 5–7).

For fixed-SST cases, z_i is insensitive to perturbations in advection (Adv$\pm$), except that S11 Adv$+$ increases LWP and thus the Sc-top entrainment driven by cloud top cooling (vice versa for Adv$-$). This effect is insignificant for S6 and S12 cases.

For fixed-OHU cases with SST feedback, z_i increases as SST rises. The increased z_i contributes to an enhanced entrainment rate at steady state, increasing the entrainment energy loss and rebalancing the energy budget. This SST effect is weaker than the effect of the subsidence perturbations, but it dominates the Adv and OHU perturbations: z_i increases with a positive energetic
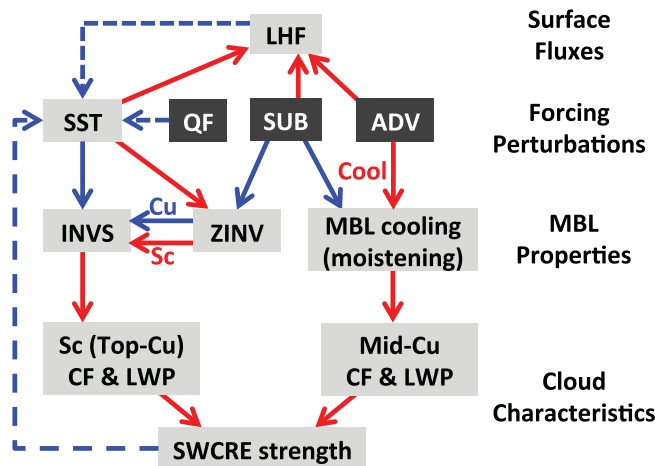

Figure 8. Schematic of the main boundary layer responses to forcing perturbations. Red arrows represent positive links (both variables change in the same direction), and blue arrows represent negative links (the two variables change in opposite directions). The dashed arrows represent responses owing to SST feedbacks that only appear with fixed OHU and interactive SST.

perturbation and an SST increase (Adv– and OHU–), and vice versa.

5.4. Inversion Strength Increases With SST and Changes With Inversion Height

The inversion strength (INVS) is defined as the jump of potential temperature θ between $z_i \pm 250$ m. Analogous to *Wood and Bretherton* [2006], it can be decomposed as

$$
\begin{aligned}
\text{INVS} &\approx \theta(z_i^+) - \theta(z_i^-) \approx \left[\theta_r(z^+) - \frac{d\theta_r}{dz}(z^+ - z_i) \right] - \left[\theta_s + \frac{d\theta}{dz} z_i \right] \\
&= \left[\theta_r(z^+) - \frac{d\theta_r}{dz} z^+ \right] - \theta_s + \left[\frac{d\theta_r}{dz} - \frac{d\theta}{dz} \right] z_i.
\end{aligned}
\tag{14}
$$

Here z_+ is some fixed height in the free troposphere (e.g., 3 km), and thus the first bracket is a constant. INVS depends on the second and third terms, i.e., the surface potential temperature θ_s, inversion height z_i, and $d\theta/dz$ in the boundary layer. Generally, $(d\theta_r/dz - d\theta/dz) > 0$ because θ_r corresponds to the tropical moist adiabat.

This equation agrees with results shown in Tables (3–5). INVS decreases as SST (and thus θ_s) warms, which is dominant in the fixed-OHU experiments with interactive SST. If SST is fixed, INVS increases as z_i rises for the Sc cases. This positive relation between INVS and z_i is reversed for the S6 Cu cases (especially Sub±), because $d\theta/dz$ increases near the Cu-top as Cu-layer deepens (Figure 5, first panel).

5.5. Cloud Cover and Sc LWP Increase as Inversion Strengthens

The total cloud cover is primarily related to the top-Cu or Sc cloud fraction, which is positively correlated with INVS. For S6, experiments with negative energetic perturbation (Sub+, Adv+, and OHU+), lower SST, and shallower z_i correspond to stronger INVS and greater cloud cover, and vice versa (Table 3). The Sub– case is exceptional: its total cloud cover increases because the mid-Cu fraction increases (see next subsection).

For S11 and S12, this correlation between cloud cover and INVS is very robust, especially during the Sc-to-Cu transition (Tables 4 and 5): a strong decrease in total cloud cover is accompanied by reduction in INVS. This effect is more significant under fixed OHU, whose boundary layer is warmed by decreased SWCRE. The LWP is dominated by the Sc-layer and scales with the change of the total cloud cover, and thus it is also positively correlated with INVS.

Sc and top-Cu are also sensitive to cloud top LW cooling, which weakens if the free troposphere becomes more emissive, leading to decreases in Sc and top-Cu fractions. This LW control on cloudiness is important in climate change scenarios in which greenhouse gas concentrations change, as we discuss in the companion paper. Also, Sc cloud cover and LWP may be less dependent on INVS if the SGS diffusivity and viscosity in the LES model are limited or disabled (see Appendix A).

5.6. Cu LWP Increases as the Mid-Cu Layer Cools

The LWP of the Cu (S6) cases is mostly dependent on the cloud fraction and LWP of the mid-Cu. Perturbations that warm and stabilize the Cu-layer (Sub+ and Adv–) tend to suppress Cu convection, and thus produce smaller Cu fraction and LWP; vice versa for opposite perturbations (Table 3 and Figure 5, third panel). This effect holds for both fixed-SST and fixed-OHU cases. For the OHU+ case, the LWP decreases without change in mid-Cu fraction, probably because of the decreased z_i and surface LHF, and vice versa for OHU–.

The cooling (and moistening) due to rain evaporation are also dependent on the vertical wind shear and the formulation of the microphysics scheme. The mid-Cu fraction and LWP are thus sensitive to these uncertain factors (the mid-Cu fraction and LWP generally decrease as evaporation efficiency is reduced). This is similar to the reported sensitivity of Cu to the choice of microphysics schemes in GCMs [e.g., *Zhao et al.*, 2016].

Reduction of LW cooling can also decrease mid-Cu. Although insignificant for these cases, this effect can be important if large changes in LW emissivity or cloudiness occur aloft. For example, the smallness of S11 Cu fraction may be attributed to its overlying Sc layer, which disables the LW cooling in the Cu-layer.

5.7. Cu Precipitation Compensates for Subsidence and LHF Effects

Precipitation is significant only for S6 Cu cases. Its drying and warming effects tend to compensate for the imposed moistening and cooling: It decreases under strengthened subsidence (Sub+), compensating for the anomalous subsidence drying and warming (vice versa for Sub–); it responds weakly to advection changes (Adv±), which dry and cool (or moisten and warm) the Cu-layer. For OHU± cases, precipitation responses compensate for the moistening or drying effects caused by surface LHF changes. Therefore, precipitation strengthens with moistening perturbations as under OHU+, and vice versa for OHU–.

5.8. SWCRE Depends on Cloud Cover and LWP

The surface SWCRE is computed as the difference between actual and clear-sky SW fluxes at the surface. Its perturbations are shown in Tables 3–5.

The SWCRE response is highly sensitive to perturbations on the S11 and S12 cases. Cases involving Sc-to-Cu transitions (Sub+, Adv–, OHU–) show significant decreases in cloud cover and LWP, causing SWCRE to weaken by 40–80 W m^{-2}. Cases with opposite perturbations maintain ∼100% cloud cover (except S12 Sub–). Their SWCRE intensifies by 10–40 W m^{-2} because of the increased LWP.

Since no cloud regime transition occurs for perturbed S6 cases, the SWCRE response is weak in those cases. It is strongest for cases with the same sign of changes in cloud fraction and LWP (Sub– and Adv±). Otherwise, the change in cloud fraction dominates for the OHU± cases, while the strong decrease of LWP dominates for the Sub+ case.

5.9. SWCRE-SST Feedback Amplifies MBL Responses and Boosts Regime Transitions

The above mechanisms imply a positive feedback between SWCRE and SST for the fixed-OHU cases (leftmost column of Figure 8): weakened SWCRE results in increased SST and reduced INVS, which further decreases cloud cover and weakens SWCRE. This feedback amplifies the MBL responses to forcing perturbations under fixed OHU (as compared to fixed SST). The positive feedback is most significant for the Sc cases: SST changes by 1–2 K without regime transition, and by 3–7 K when Sc breaks up into Cu; the SWCRE responses are more than double those with fixed SST.

The SWCRE-SST feedback is also positive for the S6 Adv± and OHU± cases (SWCRE changes of the same sign as SST changes), but it is weakly negative for S6 Sub± cases, since the z_i and mid-Cu effects dominates (top left to bottom right diagonal of Figure 8).

The SWCRE-SST feedback drives regime transitions from Sc to Cu for the OHU– cases. Transitions also occur for S12 Sub– and S11 Adv– cases, while they do not occur or are incomplete with fixed SST. Although transitions can occur for Sub+ with fixed SST, the fixed-OHU transition is faster because of the SST feedback (compare cloud cover and SWCRE in Tables 4 and 5). The final state is also different for S12 Sub+: the fixed-SST case eventually evolves into a clear MBL, while the fixed-OHU case maintains a very shallow Cu layer because of its significant SST warming.

6. Discussion and Conclusion

In this study, we have presented a forcing framework for the simulation of three subtropical boundary layer cloud regimes: Sc, Sc-over-Cu, and shallow Cu. Instead of fixing SST or fixing surface fluxes, this framework couples the atmosphere to a slab ocean layer and prescribes OHU, so that the surface energy balance is closed, and a realizable statistically steady state can be reached. Four components of large-scale atmospheric forcing are formulated: large-scale subsidence, relaxation toward a tropical moist adiabat in the free troposphere, horizontal advective cooling and drying in the lower troposphere, and Coriolis acceleration. Especially the adaptive formulation of relaxation makes it more suitable for simulating cloud regime transitions and climate change scenarios.

We have tested three cases with forcings representative of summer-time subtropical MBL conditions similar to the S12, S11, and S6 cases studied in CGILS. All three low-cloud regimes reach quasi steady states by day 10, and the MBL and cloud profiles resemble the fixed-SST results. This demonstrates that the new framework can be used in a similar fashion as the CGILS framework to study MBL clouds and their response to perturbations.

Table 6. Same as Table 3, but for the S11 Fixed-OHU Tests With Reduced SGS (Appendix A)

CASE	SST	IMBAL	SHF	LHF	RAD	OHU	ZINV	INVS	LWP	CC	SWCRE
Ctl	291.8	−1.0	2.0	88.3	144.4	55	1630	14.7	50.8	99.8	−154.9
Sub+	−2.0	−11.0	−1.6	−13.5	−26.1		−464	−0.2	+32.0	+0.0	−34.8
Sub−	+0.7	+6.0	+0.9	+0.8	+7.6		+548	−0.0	−8.4	+0.1	+13.6
Adv+	−2.1	−9.2	+0.8	−11.6	−20.0		−175	+0.8	+19.3	+0.1	−24.5
Adv−	+2.0	+6.7	−0.7	+13.6	+19.6		+166	−0.9	−13.8	−0.9	+25.7
OHU+	−2.2	−9.9	−0.6	−20.2	−10.8	+20	−232	+0.6	+10.9	+0.1	−15.9
OHU−	+2.0	+7.8	+0.6	+21.8	+10.2	−20	+233	−0.7	−7.9	−0.4	+15.7

We performed perturbation experiments to investigate the sensitivity of the steady state cloud regimes to perturbations in the prescribed OHU, horizontal advection, and subsidence, and we investigated the cloud response mechanisms. With fixed OHU, some mechanisms are similar to those with fixed SST, e.g., cloud cover and Sc LWP are positively correlated with inversion strength, and Cu LWP is positively correlated with cooling in the Cu layer. However, there are also substantial differences. In particular, the SWCRE-SST feedback is unique to the fixed-OHU experiments with a closed surface energy balance. For Cu (S6) cases, the SWCRE feedback is relatively weak, and thus SST responds mostly to the imposed energetic perturbations and shifts only by about 1 K. For Sc (S11 and S12) cases, the SWCRE feedback is significant and amplifies the cloud response to perturbations: a positive SST perturbation reduces cloud cover and LWP and weakens SWCRE; this further raises SST, causing a strong positive feedback. This feedback is especially strong for Sc cases near the transition to Cu: SST increases by 3–7 K as SWCRE weakens by 40–130 W m^{-2}. Consequently, the S11 and S12 Sc cases are sensitive to OHU perturbations of ±20 W m^{-2} and advective drying and cooling perturbations of $\pm25\%$, which may result in regime transitions from Sc to Cu steady states. The regime transition can be thought of as a run-away SST-SWCRE feedback. In this case, the system is unstable to SST perturbations and continues to shift toward warmer or cooler states, until the destabilizing SWCRE feedback weakens, such as in the well-mixed Sc and pure Cu regimes. Such regime transitions generally are absent or incomplete if SST is held fixed.

The natural extension of the current study is to investigate the climate change response of low-cloud regimes within the same forcing framework. This is the topic of the companion paper, which shows that the responses of both Cu and Sc regimes to warming differ significantly under the fixed-SST and fixed-OHU frameworks.

Appendix A: Experiments With Limited Subgrid-Scale (SGS) Dissipation

K. G. Pressel et al. (submitted, 2016) shows that Sc layers are better simulated in PyCLES with WENO advection if explicit SGS diffusion is disabled above the surface layer, leaving only the numerical dissipation from the WENO schemes. Therefore, we have run additional simulations with a rescaling parameter k_D that reduces the standard Smagorinsky diffusivity and viscosity:

$$k_D = \begin{cases} 1, & z < 100 \text{ m}, \\ 2 - z/(100 \text{ m}), & 100 \text{ m} \leq z \leq 200 \text{ m}, \\ 0, & z > 200 \text{ m}. \end{cases} \tag{A1}$$

Table 7. Same as Table 3, but for the S12 Fixed-OHU Tests With Reduced SGS (Appendix A)

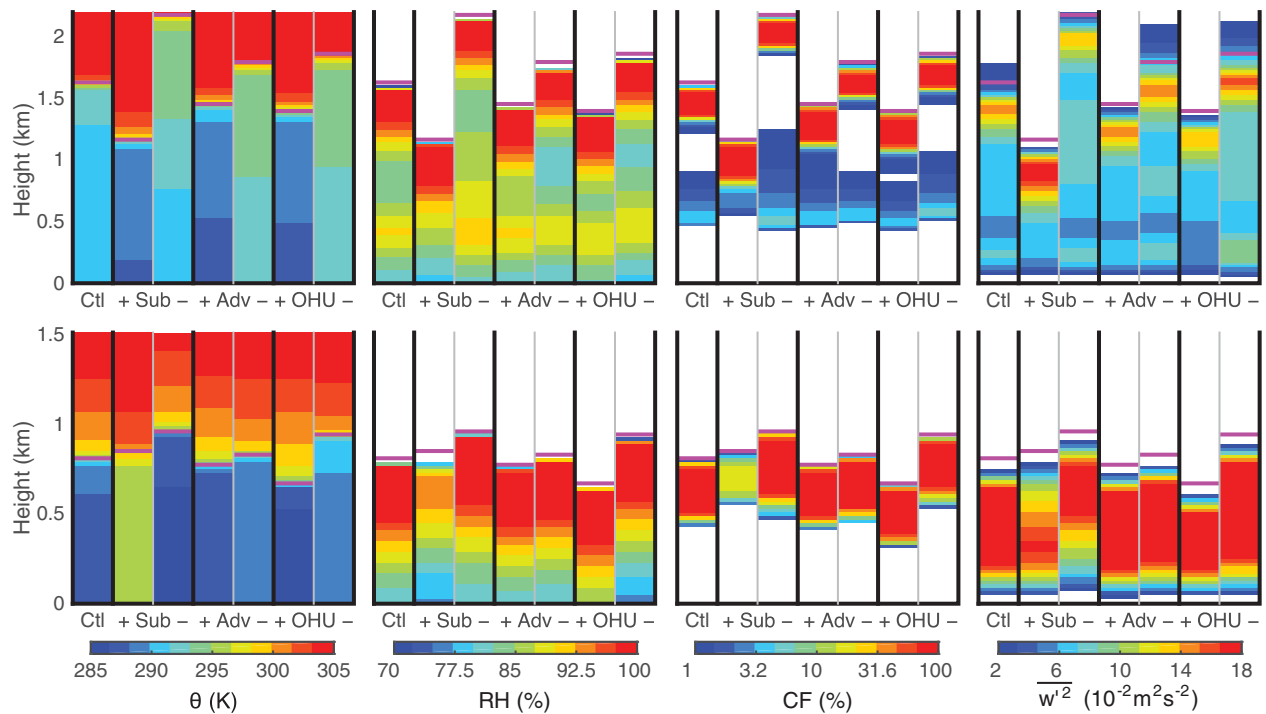| CASE	SST	IMBAL	SHF	LHF	RAD	OHU	ZINV	INVS	LWP	CC	SWCRE
Ctl	289.6	−0.4	4.3	82.3	126.2	40	810	13.6	77.5	99.6	−186.5
Sub+	+7.8	+6.6	+4.1	+85.6	+96.3		+40	−5.5	−68.6	−72.5	+155.8
Sub−	−1.8	−6.0	−3.7	−18.4	−28.1		+150	+1.2	+40.3	+0.3	−28.9
Adv+	−0.5	+0.1	+2.7	+0.2	+3.0		−36	+0.2	−4.3	−0.1	+3.3
Adv−	+0.5	+0.6	−2.5	−0.3	−2.2		+20	−0.3	+3.5	+0.0	−2.4
OHU+	−1.6	−0.5	+3.3	−17.7	+5.1	+20	−140	+0.5	−5.0	+0.1	+2.5
OHU−	+1.4	+1.2	−2.9	+17.3	−4.3	−20	+133	−0.4	+4.6	−0.1	−1.8

Figure 9. Same as Figure 5, but for the S11 (top) and S12 (bottom) fixed-OHU sensitivity tests with reduced SGS diffusivity (Appendix A).

Therefore, SGS diffusivity and viscosity are zero above 200 m. The S11 and S12 control and perturbed simulations are run at the same resolution with this SGS limiter.

As shown in Tables 6 and 7, the model with SGS limiter (aka SGSlim) produces much larger LWP than the standard model. Therefore, the SWCRE is much stronger. The prescribed OHU thus needs to be reduced in accordance with the weakened surface SW heating. The selected values are 55 W m^{-2} for S11 and 40 W m^{-2} for S12.

The results of fixed-OHU perturbed cases are also shown in Tables 6 and 7, as well as in Figure 9. For S11, the change in SWCRE is stronger than the direct energetic perturbations, and thus SST changes in the same direction as SWCRE. This positive SST-SWCRE feedback is similar to that with the standard model. However, the SWCRE and SST changes in Sub± cases are opposite to those with the standard model, possibly because of an inversion height effect: cases with deeper inversion (e.g., Sub–) are more decoupled with less LWP, and vice versa. This inversion height effect is not seen from S11 Sub± cases in the standard model. Also, all perturbed cases maintain their Sc-layers, and the transition to Cu does not occur with the perturbations we considered.

For S12, the change in SWCRE is very small and acts as a negative feedback for Adv± and OHU± cases (i.e., the SWCRE change is opposite to SST change). Although changes in inversion height and strength are similar to the standard model, the LWP response is reversed. This feedback may be caused by other processes, such as the LHF and advective drying perturbations that change the MBL moisture budget. Further analysis is needed to identify this weak SWCRE feedback. In contrast, the SWCRE-SST feedback is strongly positive for the Sub± cases, and Sub+ warms and breaks up into Cu. In contrast to the standard model, the Sub– case does not become decoupled, and thus it shows strengthened SWCRE and decreased SST.

References

Ackerman, A. S., et al. (2009), Large-eddy simulations of a drizzling, stratocumulus-topped marine boundary layer, *Mon. Weather Rev.*, *137*, 1083–1110, doi:10.1175/2008MWR2582.1.

Allen, M. R., and W. J. Ingram (2002), Constraints on future changes in climate and the hydrologic cycle, *Nature*, *419*, 224–232, doi:10.1038/nature01092.

Arakawa, A., and V. R. Lamb (1977), Computational design of the basic dynamical processes of the UCLA general circulation model, in *General Circulation Models of the Atmosphere, Methods Comput. Phys. Adv. Res. Appl.*, vol. *17*, edited by J. Chang, pp. 173–265, Academic, N. Y., doi:10.1016/B978-0-12-460817-7.50009-4.

Balsara, D. S., and C.-W. Shu (2000), Monotonicity preserving weighted essentially non-oscillatory schemes with increasingly high order of accuracy, *J. Comput. Phys.*, *160*, 405–452, doi:10.1006/jcph.2000.6443.

Bellon, G., and B. Stevens (2012), Using the sensitivity of large-eddy simulations to evaluate atmospheric boundary layer models, *J. Atmos. Sci.*, *69*, 1582–1601, doi:10.1175/JAS-D-11-0160.1.

Blossey, P. N., C. S. Bretherton, M. Zhang, A. Cheng, S. Endo, T. Heus, Y. Liu, A. P. Lock, S. R. de Roode, and K.-M. Xu (2013), Marine low cloud sensitivity to an idealized climate change: The CGILS LES intercomparison, *J. Adv. Model. Earth Syst.*, *5*, 234–258, doi:10.1002/jame.20025.

Boer, G. J. (1993), Climate change and the regulation of the surface moisture and energy budgets, *Clim. Dyn.*, *8*, 225–239, doi:10.1007/BF00198617.

Bony, S., and J.-L. Dufresne (2005), Marine boundary layer clouds at the heart of tropical cloud feedback uncertainties in climate models, *Geophys. Res. Lett.*, *32*, L20806, doi:10.1029/2005GL023851.

Bretherton, C. S. (2015), Insights into low-latitude cloud feedbacks from high-resolution models, *Philos. Trans. R. Soc. A*, *373*, 20140415, doi:10.1098/rsta.2014.0415.

Bretherton, C. S., P. N. Blossey, and C. R. Jones (2013), Mechanisms of marine low cloud sensitivity to idealized climate perturbations: A single-LES exploration extending the CGILS cases, *J. Adv. Model. Earth Syst.*, *5*, 316–337, doi:10.1002/jame.20019.

Brient, F., and T. Schneider (2016), Constraints on climate sensitivity from space-based measurements of low-cloud reflection, *J. Clim.*, *29*, 5821–5835, doi:10.1175/JCLI-D-15-0897.1.

Brient, F., T. Schneider, Z. Tan, S. Bony, X. Qu, and A. Hall (2015), Shallowness of tropical low clouds as a predictor of climate models' response to warming, *Clim. Dyn.*, *47*, 433–449, doi:10.1007/s00382-015-2846-0.

Byun, D. W. (1990), On the analytical solutions of flux-profile relationships for the atmospheric surface layer, *J. Appl. Meteorol.*, *29*, 652–657, doi:10.1175/1520-0450(1990)029 < 0652:OTASOF>2.0.CO;2.

Caldwell, P., and C. S. Bretherton (2009a), Large eddy simulation of the diurnal cycle in Southeast Pacific stratocumulus, *J. Atmos. Sci.*, *66*, 432–449, doi:10.1175/2008JAS2785.1.

Caldwell, P., and C. S. Bretherton (2009b), Response of a subtropical stratocumulus-capped mixed layer to climate and aerosol changes, *J. Clim.*, *22*, 20–38, doi:10.1175/2008JCLI1967.1.

Cess, R. D., et al. (1990), Intercomparison and interpretation of climate feedback processes in 19 atmospheric general circulation models, *J. Geophys. Res.*, *95*, 16,601–16,615, doi:10.1029/JD095iD10p16601.

Cess, R. D., et al. (1996), Cloud feedback in atmospheric general circulation models: An update, *J. Geophys. Res.*, *101*, 12,791–12,794, doi:10.1029/96JD00822.

Charney, J. G. (1963), A note on large-scale motions in the tropics, *J. Atmos. Sci.*, *20*, 607–609, doi:10.1175/1520-0469(1963)020 < 0607:ANOLSM>2.0.CO;2.

Chung, D., G. Matheou, and J. Teixeira (2012), Steady-state large-eddy simulations to study the stratocumulus to shallow cumulus cloud transition, *J. Atmos. Sci.*, *69*, 3264–3276, doi:10.1175/JAS-D-11-0256.1.

Dee, D. P., et al. (2011), The ERA-Interim reanalysis: Configuration and performance of the data assimilation system, *Q. J. R. Meteorol. Soc.*, *137*, 553–597, doi:10.1002/qj.828.

Dufresne, J.-L., and S. Bony (2008), An assessment of the primary sources of spread of global warming estimates from coupled atmosphere–ocean models, *J. Clim.*, *21*, 5135–5144, doi:10.1175/2008JCLI2239.1.

Duynkerke, P. G., P. J. Jonker, A. Chlond, M. C. Van Zanten, J. Cuxart, P. Clark, E. Sanchez, G. Martin, G. Lenderink, and J. Teixeira (1999), Intercomparison of three- and one-dimensional model simulations and aircraft observations of stratocumulus, *Boundary Layer Meteorol.*, *92*, 453–487, doi:10.1023/A:1002006919256.

Frierson, D. M. W., I. M. Held, and P. Zurita-Gotor (2006), A gray-radiation aquaplanet moist GCM. Part I: Static stability and eddy scale, *J. Atmos. Sci.*, *63*, 2548–2566, doi:10.1175/JAS3753.1.

Held, I. M., and B. J. Soden (2000), Water vapor feedback and global warming, *Annu. Rev. Energy Environ.*, *25*, 441–475, doi:10.1146/annurev.energy.25.1.441.

Held, I. M., and B. J. Soden (2006), Robust responses of the hydrological cycle to global warming, *J. Clim.*, *19*, 5686–5699, doi:10.1175/JCLI3990.1.

Heus, T., et al. (2010), Formulation of the dutch atmospheric large-eddy simulation (DALES) and overview of its applications, *Geosci. Model Dev.*, *3*, 415–444, doi:10.5194/gmd-3-415-2010.

Iacono, M. J., J. S. Delamere, E. J. Mlawer, M. W. Shephard, S. A. Clough, and W. D. Collins (2008), Radiative forcing by long-lived greenhouse gases: Calculations with the AER radiative transfer models, *J. Geophys. Res.*, *113*, D13103, doi:10.1029/2008JD009944.

Jiang, G.-S., and C.-W. Shu (1996), Efficient implementation of weighted ENO schemes, *J. Comput. Phys.*, *126*, 202–228, doi:10.1006/jcph.1996.0130.

Kalmus, P., M. Lebsock, and J. Teixeira (2014), Observational boundary layer energy and water budgets of the stratocumulus-to-cumulus transition, *J. Clim.*, *27*, 9155–9170, doi:10.1175/JCLI-D-14-00242.1.

Knutson, T. R., and S. Manabe (1995), Time-mean response over the tropical Pacific to increased CO_2 in a coupled ocean-atmosphere model, *J. Clim.*, *8*, 2181–2199, doi:10.1175/1520-0442(1995)008 < 2181:TMROTT>2.0.CO;2.

Lilly, D. K. (1962), On the numerical simulation of buoyant convection, *Tellus*, *14*, 148–172, doi:10.1111/j.2153-3490.1962.tb00128.x.

Liu, X.-D., S. Osher, and T. Chan (1994), Weighted essentially non-oscillatory schemes, *J. Comput. Phys.*, *115*, 200–212, doi:10.1006/jcph.1994.1187.

Matheou, G., D. Chung, L. Nuijens, B. Stevens, and J. Teixeira (2011), On the fidelity of large-eddy simulation of shallow precipitating cumulus convection, *Mon. Weather Rev.*, *139*, 2918–2939, doi:10.1175/2011MWR3599.1.

O'Gorman, P. A., and T. Schneider (2008), The hydrological cycle over a wide range of climates simulated with an idealized GCM, *J. Clim.*, *21*, 3815–3832, doi:10.1175/2007JCLI2065.1.

Pauluis, O. (2008), Thermodynamic consistency of the anelastic approximation for a moist atmosphere, *J. Atmos. Sci.*, *65*, 2719–2729, doi:10.1175/2007JAS2475.1.

Pressel, K. G., C. M. Kaul, T. Schneider, Z. Tan, and S. Mishra (2015), Large-eddy simulation in an anelastic framework with closed water and entropy balances, *J. Adv. Model. Earth Syst.*, *7*, 1425–1456, doi:10.1002/2015MS000496.

Rieck, M., L. Nuijens, and B. Stevens (2012), Marine boundary layer cloud feedbacks in a constant relative humidity atmosphere, *J. Atmos. Sci.*, *69*, 2538–2550, doi:10.1175/JAS-D-11-0203.1.

Sandu, I., and B. Stevens (2011), On the factors modulating the stratocumulus to cumulus transitions, *J. Atmos. Sci.*, *68*, 1865–1881, doi:10.1175/2011JAS3614.1.

Schneider, T., P. A. O'Gorman, and X. J. Levine (2010), Water vapor and the dynamics of climate changes, *Rev. Geophys.*, *48*, RG3001, doi:10.1029/2009RG000302.

Seifert, A. (2008), On the parameterization of evaporation of raindrops as simulated by a one-dimensional rainshaft model, *J. Atmos. Sci.*, *65*, 3608–3619, doi:10.1175/2008JAS2586.1.

Seifert, A., and K. D. Beheng (2001), A double-moment parameterization for simulating autoconversion, accretion and selfcollection, *Atmos. Res.*, *59–60*, 265–281, doi:10.1016/S0169-8095(01)00126-0.

Seifert, A., and K. D. Beheng (2006), A two-moment cloud microphysics parameterization for mixed-phase clouds. Part 1: Model description, *Meteorol. Atmos. Phys.*, *92*, 45–66, doi:10.1007/s00703-005-0112-4.

Shu, C.-W., and S. Osher (1988), Efficient implementation of essentially non-oscillatory shock-capturing schemes, *J. Comput. Phys.*, *77*, 439–471, doi:10.1016/0021-9991(88)90177-5.

Siebesma, A. P., et al. (2003), A large eddy simulation intercomparison study of shallow cumulus convection, *J. Atmos. Sci.*, *60*, 1201–1219, doi:10.1175/1520-0469(2003)60>1201: ALESIS>2.0.CO;2.

Smagorinsky, J. (1963), General circulation experiments with the primitive equations. 1: The basic experiment, *Mon. Weather Rev.*, *91*, 99–164, doi:10.1175/1520-0493(1963)091 < 0099:GCEWTP>2.3.CO;2.

Sobel, A. H., J. Nilsson, and L. M. Polvani (2001), The weak temperature gradient approximation and balanced tropical moisture waves, *J. Atmos. Sci.*, *58*, 3650–3665, doi:10.1175/1520-0469(2001)058 < 3650:TWTGAA>2.0.CO;2.

Stephens, G. L., and T. D. Ellis (2008), Controls of global-mean precipitation increases in global warming GCM experiments, *J. Clim.*, *21*, 6141–6155, doi:10.1175/2008JCLI2144.1.

Stevens, B. (2005), Atmospheric moist convection, *Annu. Rev. Earth Planet. Sci.*, *33*, 605–643, doi:10.1146/annurev.earth.33.092203.122658.

Stevens, B., and A. Seifert (2008), Understanding macrophysical outcomes of microphysical choices in simulations of shallow cumulus convection, *J. Meteorol. Soc. Jpn. Ser. II*, *86A*, 143–162, doi:10.2151/jmsj.86A.143.

Stevens, B., et al. (2005), Evaluation of large-eddy simulations via observations of nocturnal marine stratocumulus, *Mon. Weather Rev.*, *133*, 1443–1462, doi:10.1175/MWR2930.1.

Teixeira, J., et al. (2011), Tropical and subtropical cloud transitions in weather and climate prediction models: The GCSS/WGNE Pacific cross-section intercomparison (GPCI), *J. Clim.*, *24*, 5223–5256, doi:10.1175/2011JCLI3672.1.

vanZanten, M. C., et al. (2011), Controls on precipitation and cloudiness in simulations of trade-wind cumulus as observed during RICO, *J. Adv. Model. Earth Syst.*, *3*, M06001, doi:10.1029/2011MS000056.

Vial, J., J.-L. Dufresne, and S. Bony (2013), On the interpretation of inter-model spread in CMIP5 climate sensitivity estimates, *Clim. Dyn.*, *41*, 3339–3362, doi:10.1007/s00382-013-1725-9.

Webb, M. J., and A. P. Lock (2013), Coupling between subtropical cloud feedback and the local hydrological cycle in a climate model, *Clim. Dyn.*, *41*, 1923–1939, doi:10.1007/s00382-012-1608-5.

Webb, M. J., et al. (2006), On the contribution of local feedback mechanisms to the range of climate sensitivity in two GCM ensembles, *Clim. Dyn.*, *27*, 17–38, doi:10.1007/s00382-006-0111-2.

Wood, R. (2012), Stratocumulus clouds, *Mon. Weather Rev.*, *140*, 2373–2423, doi:10.1175/MWR-D-11-00121.1.

Wood, R., and C. S. Bretherton (2006), On the relationship between stratiform low cloud cover and lower-tropospheric stability, *J. Clim.*, *19*, 6425–6432, doi:10.1175/JCLI3988.1.

Zhang, M., and C. Bretherton (2008), Mechanisms of low cloud–climate feedback in idealized single-column simulations with the community atmospheric model, version 3 (CAM3), *J. Clim.*, *21*, 4859–4878, doi:10.1175/2008JCLI2237.1.

Zhang, M., C. S. Bretherton, P. N. Blossey, S. Bony, F. Brient, and J.-C. Golaz (2012), The CGILS experimental design to investigate low cloud feedbacks in general circulation models by using single-column and large-eddy simulation models, *J. Adv. Model. Earth Syst.*, *4*, M12001, doi:10.1029/2012MS000182.

Zhang, M., et al. (2013), CGILS: Results from the first phase of an international project to understand the physical mechanisms of low cloud feedbacks in single column models, *J. Adv. Model. Earth Syst.*, *5*, 826–842, doi:10.1002/2013MS000246.

Zhao, M., et al. (2016), Uncertainty in model climate sensitivity traced to representations of cumulus precipitation microphysics, *J. Clim.*, *29*, 543–560, doi:10.1175/JCLI-D-15-0191.1.